On the fluid dynamics of spin-over in a partially filled cylinder

Gergana G. Atanasova ⓘ ; Christian A. Klettner ⓘ ; Martina Micheletti ⓘ ; Andrea Ducci ✉ ⓘ

Check for updates

View Online

Export Citation

Articles You May Be Interested In

On the fluid dynamics of spin-over in a partially filled cylinder

View Online   Export Citation   CrossMark

Gergana G. Atanasova,[1] (iD) Christian A. Klettner,[2] (iD) Martina Micheletti,[1] (iD) and Andrea Ducci[2,a] (iD)

AFFILIATIONS

[1]Biochemical Engineering Department, University College London, Gower Street, London WC1E 6BT, United Kingdom
[2]Mechanical Engineering Department, University College London, Gower Street, London WC1E 7JE, United Kingdom

[a]Author to whom correspondence should be addressed: a.ducci@ucl.ac.uk

ABSTRACT

This work provides a comprehensive account of the flow within a cylinder with a free surface and an intermediate aspect ratio (liquid height to cylinder radius, $L/R = 0.5$), undergoing spin-over: the rotation of the entire cylinder about its vertical axis is impulsively reversed from solid body rotation to the same angular velocity in the opposite direction. The transient unstable fluid flow arising from this has not previously been characterized. This study employs two-dimensional, two-component particle image velocimetry, planar laser-induced fluorescence, and three-dimensional computational fluid dynamics side by side to capture the spin-over process in full. A thorough investigation of the fluid flow established within the bulk of the fluid, as well as in the endwall and sidewall boundary layers, is provided to reveal the intricate interplay between those regions in time. The investigation goes through the various flow stages during spin-over, including the primary and secondary endwall boundary layer separations, the generation of type I/type II waves, and the behavior of the Taylor–Görtler vortices in the sidewall boundary layer, as well as the late-stage establishment of geostrophic flow through Ekman pumping. The impact of increasing the Reynolds number, Re, and Froude number, Fr, is also investigated ($2504 < Re < 25\,043$; $0.02 < Fr < 1.07$), shedding light on secondary endwall boundary layer separations and the onset of three-dimensional turbulence. The findings have implications for diverse fields, from the fluid dynamics in rotating bioreactors to geophysical and astrophysical systems.

I. INTRODUCTION

The physics of a fluid adapting to the changing rotation rate of a bounding vertical cylinder has found practical application in a number of fields, including ballistics,[1] aerospace engineering,[2] oceanography,[3] and turbomachinery,[4] to mention a few. Recently, it has also become relevant to bioprocess engineering and Advanced Therapy Medicinal Products (ATMPs) manufacturing, with the release of the CliniMACS Prodigy® (Miltenyi Biotec) platform for the automated production of CAR-T cell therapy, a personalized cell-based gene therapy, which offers a single-dose cure to multiple forms of advanced cancer.[5–7] At the core of the system's functionality is its bioreactor unit, the CentriCult™ chamber: an intermediate aspect ratio, partially filled cylinder with quiescent liquid height to container radius ratio, $L/R = 0.5$, rotating intermittently about its central vertical axis. From a bioprocessing perspective, this represents a new type of bioreactor in terms of flow patterns, mixing, shear stress, and power consumption, as it uses intermittent rotation of the entire cylindrical container to agitate, homogenize, and suspend the cell culture during the expansion phase[8]

without an impeller or any other internals.[9] From a fluid dynamics perspective, the transient flows generated within the bioreactor by the intermittent rotation are spin-up from rest (start), spin-down to rest (stop), and spin-over (reversal of the direction of rotation), each of which is characterized by different flow features with direct implications for cell proliferation.

The flow dynamics of spin-up (with or without a free surface) and spin-down (mainly without a free surface) in a cylindrical container have been topics of research for years, however, spin-over, namely the focus of this study, is not well documented, especially for partially filled configurations. As a consequence, the following literature review focuses first on the processes of spin-up from rest and spin-down to rest from solid body rotation (SBR) in a cylinder, as they provide useful insight into the relevant fluid dynamics and lay the foundations for studying spin-over in a cylinder. While the transient behavior of the fluid in spin-over confined to a cylindrical enclosure remains unknown, similar problems have been examined, under varying other boundary conditions (i.e., a single rotating disk in a counter-

rotating fluid, two parallel coaxial counter-rotating disks, and a rotating cylindrical enclosure with a counter-rotating top endwall), which all bear similarities to the current case of interest and will be examined in the second part of the literature review.

For a rotating cylinder, it is commonly accepted to use the definition of the Reynolds number, Re, employed for the flow over a rotating disk[10]

$$Re = \frac{\Omega R^2}{\nu}, \tag{1}$$

where Ω is the angular velocity of a cylinder of radius, R, rotating about its vertical axis, and ν is the kinematic viscosity of the fluid. The boundary layer flow remains laminar for $Re < 3 \times 10^5$.[11] Two additional dimensionless numbers are important: the Rossby number,

$$\varepsilon = \frac{\Delta\Omega}{\Omega}, \tag{2}$$

which quantifies the relative change in angular velocity of the cylinder, and, for free surface flows, the Froude number, Fr,

$$Fr = \frac{\Omega^2 R^2}{gL}, \tag{3}$$

where g is the gravitational acceleration, and L is the quiescent liquid height.

Non-linear spin-up (i.e., spin-up from rest, $\varepsilon = 1$) in a cylinder was first addressed by Wedemeyer,[12] who extended the founding theory laid down by Greenspan and Howard[13] for linear spin-up (i.e., $\varepsilon \ll 1$). They considered high aspect ratio completely filled cylinders (container height to radius ratio, $H/R > 4$), and showed that within the first few radians of rotation, a viscous boundary layer of the von Kármán type develops at the endwell, and a Stewartson type boundary layer at the sidewall, where mass transfer occurs, while the interior of the fluid remains inviscid. The endwall boundary (Ekman) layer at the endwall expels fluid radially outward under the effect of centrifugal forces. To balance the mass displaced, a small axial influx is drawn into the boundary layer from the inviscid interior above, a convection process known as Ekman pumping. They also showed that the Ekman pumping mechanism results in geostrophic flow, dividing the fluid into an outer rotating and an inner non-rotating domain. The boundary between rotating and non-rotating fluid is a vertical shear front of tangential velocity, which propagates radially inward from the sidewall to the axis of rotation. According to Wedemeyer's model for a completely filled cylinder, the radial location of the vertical shear front follows an exponential decay law in Ekman time, T,

$$T = t\left(\frac{\nu\Omega}{H^2}\right)^{1/2} = \Omega t\left(\frac{R}{H}\right)Re^{-1/2}, \tag{4}$$

where t is the dimensional time and H is the vertical height of a completely filled cylinder. In the case of cylinders with a free surface, the convention is to use $H = 2L$, since the flow in a completely filled cylinder is symmetric with respect to the horizontal midplane (an Ekman boundary layer forms on each endwall), while in a partially filled cylinder, only the bottom endwall Ekman layer exists.[14] Wedemeyer's solution for completely filled high aspect ratio ($H/R > 4$) cylinders has been confirmed experimentally[15,16] and computationally[17,18] and has also been extended to cylinders with a free

surface[1,19] by considering additional axial and radial velocity components induced in proximity of the free surface by its deformation.[14] In the presence of a free surface, the propagation of the tangential velocity shear front is slower, with a corresponding increase in the characteristic Ekman timescale with increasing Froude number for linear spin-up.[13,20,21] These findings have been experimentally confirmed for (non-linear) spin-up from rest in an intermediate aspect ratio cylinder ($L/R = 0.5$) with a free surface.[22] Neither spin-up nor spin-down are characterized by a free surface exhibiting oscillations, breaking waves, and/or turbulence generation as in the case of thin films over topographies.[23,24]

For small changes in the rotation rate, i.e., the linear problem of spin-down is essentially the same as that for linear spin-up ($\varepsilon \ll 1$); however, spin-down to rest ($\varepsilon = -1$) is significantly different. In the context of impulsive spin-down to rest it is first important to mention that for a finite cylinder, such as the case considered in this work, there is no analytical solution since the flow is dominated by Ekman convection and is strongly nonlinear.[25] However, in the absence of endwall boundary layers (or a free surface), i.e., for impulsive spin-down to rest in an infinite cylinder,[26,27] there is no generation of Ekman convection, and the problem can be approached analytically.

When the rotation rate of a finite cylinder is impulsively brought to rest, the endwall boundary layer formed is of the Bödewadt type, characterized by a radial inflow along the endwall balanced by an axial efflux from the Ekman layer into the inviscid interior above. This generates a similar pumping mechanism to spin-up but in the opposite direction. However, the main difference in the two non-linear processes arises from the flow characteristics of the sidewall boundary layer. On the one hand during spin-up, it is classified as a Stewartson boundary layer, which carries on the (radial) mass transport from the Ekman layer axially upward along the sidewall.[28] On the other hand during spin-down, the curvature of the cylinder wall causes the generation of a centrifugal instability, which takes the form of counter-rotating vortex pairs, known as Taylor–Görtler (T–G) vortices. These occur when $Re > Re_{crit}$, where Re_{crit} varies in the literature between $140 < Re_{crit} < 320$[25,29–31] and in the first instance after formation are similar to those produced in a Taylor–Couette flow, when the outer cylinder is stationary. Euteneuer[32,33] studied their formation experimentally in a completely filled high aspect ratio cylinder ($H/R = 4$), using reflective flakes to visualize them on the sidewall, and showed that their onset time and wavelength are scalable with Re. These findings have been confirmed experimentally for high aspect ratios ($H/R > 4$)[29,34] and computationally in infinitely long cylinders.[25,27] For the latter case, Kim and Choi[31] have derived an analytical model for the onset time and wavelength of the T–G vortices in close agreement with experimental data in the literature. The primary vortex pairs grow and propagate away from the sidewall before merging to form larger pairs, at which point the boundary layer transitions to turbulence.[27] As observed computationally this transition further enhances the loss of angular momentum of the bulk flow.[25] Atanasova et al.[22,35] have examined, from a bioprocessing perspective, spin-down from solid body rotation and spin-down from different levels of spin-up before SBR is reached, respectively.

Aside from the instability of the sidewall boundary layer, the endwall boundary (Bödewadt) layer during spin-down is also prone to instabilities. Two distinct wave types have been reported in the literature: stationary spiral (type I) and propagating circular (type II) waves.

The presence of these waves was first reported for the boundary layer on a rotating disk,[36,37] where a comprehensive numerical study was presented alongside dye visualization experiments, showing that both von Kármán and Bödewadt boundary layers become unstable at $Re > Re_{crit} = 70$ and $Re_{crit} = 15$, respectively. It was also reported that the interaction of those wave types promoted a premature transition to turbulence in Bödewadt boundary layers. Type I and type II waves were experimentally studied in the context of a completely filled cylinder ($H/R = 2$) spinning down to rest.[38,39] These works visualized the same modes of wave instabilities with reflective flakes but reported a significantly higher value of $Re_{crit} \approx 625$ for the Bödewadt boundary layer in a cylinder. Their LDA measurements of the tangential velocity component showed that the flow perturbations associated with the waves are not confined to the boundary layer but propagate into the interior. These findings were confirmed computationally and experimentally with reflective flakes,[40] by characterizing these type II (spiral) instabilities for different aspect ratios ($0.5 < H/R < 8$). It was found that the spiral waves persist longer for higher Re, are spatially broader, have lower amplitude, and travel more slowly in smaller aspect ratios, but they always decay for spin-down to rest and do not significantly affect the overall flow.

To the best of the author's knowledge, no account of the mechanism of adaptation of the fluid to the new opposite rotation rate of a partially or completely filled cylinder (i.e., spin-over) has been given in the literature. Nevertheless, insight can be gained from various other configurations, which are reviewed hereafter.

The transient boundary layer flow over a finite rotating disk in a counter-rotating fluid, after its angular velocity, Ω, is impulsively reversed to $-\Omega$ at $t = 0$, was studied analytically[41–43] and numerically.[44] All studies agree that at $\Omega t = 2.36$ the boundary layer develops a singularity at the axis of rotation. While their studies were focused on the boundary layer alone, Stewartson et al.[43] remarked that the effect of this singularity would also impact the core flow above the boundary layer.

Another flow configuration with analogies to the spin-over process in a cylinder is that of fluid placed in between two parallel disks, rotating in opposite directions about a common axis. Pearson[45] carried out computations for the case in which two infinite disks are separated by a finite distance, H, and are impulsively started from rest in opposite directions ($Re = 100$ and 1000). They reported that at $Re = 1000$ no stable symmetric flow exists between the two disks and that it is possible for the fluid to exceed the angular velocity of either disk. In the case of two parallel disks, an additional dimensionless parameter is defined, s,

$$s = \frac{\Omega_1}{\Omega_2}, \tag{5}$$

which is the ratio of the angular velocities of the two disks. If $s = 0$, one of the disks is stationary, and for $s < 0$, they are rotating in opposite directions. Dijkstra and Heijst[46] investigated the flow dynamics in the confined space between two closely positioned parallel disks with a narrow gap ($H/R = 0.07$) through both numerical simulations and experimental stereo-photography, employing polystyrene spheres as seeding particles. Despite the closed configuration, this arrangement precludes the development of core flow due to the minimal gap between the disks, which leads exclusively to boundary layer flow. Their analysis encompassed Reynolds numbers below 100 and angular

velocity ratios, $-0.8 < s < 0$, indicative of weak counter-rotation. Their findings demonstrated that the boundary layer at the slower disk separates, due to the existence of a stagnation point at which the radial component of the velocity is 0. The boundary layer separation produces a two-cell flow structure within the geometry. They reported that the stagnation point radial coordinate was dependent on both the ratio of rotation to counter rotation, s, and the Reynolds number, Re. In a similar configuration ($H/R = 0.05$), Gauthier et al.[47] studied the instabilities generated in the boundary layers of each disk using reflective flakes. They provided a comprehensive report on the different types of instabilities present for counter-rotation ratios, $-1 < s < 0$, including propagating axisymmetric and stationary spiral waves, similar to the type I/type II waves in Bödewadt boundary layers, as well as "negative spirals" at the slower disk.

Finally, perhaps the most relevant studies to the spin-over flow in a cylinder considered in this work, are those presented by Lopez[48] and Lopez et al.[49] They addressed the flow computationally in a completely filled cylinder of intermediate aspect ratio ($H/R = 0.5$), rotating about its vertical axis, bounded by a counter-rotating disk at the top. The time-independent numerical solution for this configuration was computed for a range of aspect ratios, $0.125 \leq H/R \leq 0.5$, Reynolds numbers, $300 \leq Re \leq 3000$, and rotation ratios, $-3 \leq s \leq 0$, where Ω_2 and Ω_1 are the angular velocity of the cylinder and of the counter-rotating top endwall, respectively. Lopez[48] found that when the cylinder height is no longer small in comparison to the radius, i.e., $0.25 < H/R < 0.5$, the core flow is strongly dependent on the boundary layer separation near the counter-rotating disk, also reported by Dijkstra and Heijst.[46] For $Re = 3000$ and $-2.7 < s < 0$, Lopez[48] reported that this boundary layer was separated and formed a free shear layer, which affected the interior flow. Two steady flow configurations were identified, depending on whether the separated boundary layer merged with that at the bottom of the cylinder, or reattached to the counter-rotating top plate. The flow dynamics for strong counter-rotation, $s < -2.7$, are characterized by an unstable oscillating free shear layer, which was seen to "flip-flop" between the top plate and the cylinder base, with an intermediate phase when it was attached to neither boundary layer.

Based on the review above it is evident that some relevant literature exists on spin-over phenomena in different configurations from the one addressed in the current study; however, a certain gap in the understanding persists, particularly around the spin-over of confined flows. Furthermore, the majority of studies focus on very small aspect ratios ($H/R \leq 0.1$), where only boundary layer flow develops, without interior flow, and very few works focus on transient spin-over problems where the fluid is experiencing adaptation from one steady state to another, as opposed to time-independent counter-rotation. In addition, no studies were found which examine spin-over phenomena in partially filled containers, which are typically encountered in bioreactors. Bioreactor geometries for the production of ATMPs, as the one considered in this work, are often characterized by intermediate aspect ratio configurations ($0.25 \leq L/R \leq 1$) with a free surface. This configuration offers a parameter space, where boundary layer instabilities on both the endwall and sidewall of the cylinder are allowed to form and interact with each other, while the interior fluid is characterized by a convective (core) flow.

The present study addresses some of the gaps in the spin-over literature by investigating the intricate secondary flow structures and

boundary layer behaviors during spin-over in a partially filled cylinder with an intermediate aspect ratio of liquid height to radius, $L/R = 0.5$, and an angular velocity ratio before and after inverting the rotation of the entire cylinder, $s = -1$. A combination of experimental techniques, including particle image velocimetry (PIV) and planar laser-induced fluorescence (PLIF), as well as a transient three-dimensional (3D) direct numerical simulation (DNS), were used to study the flow for $2500 < Re < 25043$. Novel data are presented which sheds light on the complex transient fluid mechanics occurring in the vessel as the fluid adapts to the reversal of rotation of the cylinder. The present study improves the understanding of the endwall boundary layer behavior during spin-over and the development of secondary circulations. It also gives an account of the coexisting Taylor–Görtler (T–G) vortices in the sidewall boundary layer. The insight generated can be used for optimizing the operation of the intermittently rotating cylinder bioreactor, and thus lead to higher yields through the adoption of improved agitation strategies.

II. METHODOLOGY

A. Experimental setup

A transparent plexiglass cylindrical container was used for the experiments, with a radius, $R = 49$ mm, partially filled with ultrapure water to a liquid height, $L = 25$ mm to replicate the geometry of the CentriCult^{TM} bioreactor. The experimental setup is shown in Fig. 1. The cylinder, rotated by a motor attached on top, was submerged into a larger square tank of water to minimize the optical distortion due to refraction at the curved cylindrical wall. The axis of rotation was fixed
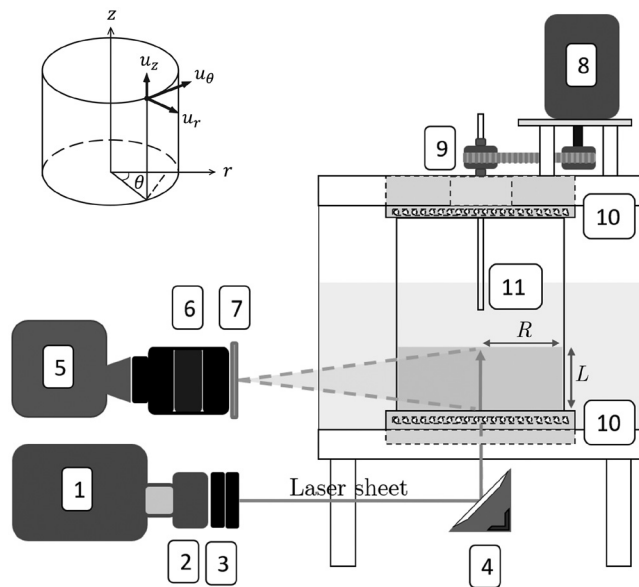
FIG. 1. Experimental setup: (1) Continuous diode-pumped solid-state (DPSS) green laser, 532 nm, 3.6 W (Laserglow Technologies, LRS-0532 Series); (2) spherical lens; (3) two cylindrical lenses in series, 25 mm (left) and 15 mm (right); (4) mirror at 45° to laser sheet; (5) high-speed camera, 7400 fps at 1 MP (Phantom VEO 710); (6) Micro-NIKKOR 105 mm f/2.8G IF-ED lens (Nikon); (7) monochromatic light filter; (8) low-inertia servo motor (MPL-A320 series, Allen Bradley); (9) belt-driven rotation mechanism; (10) ball bearings; and (11) tube for injection of liquids along the vertical axis, while the cylinder is in rotation.

TABLE I. Range of operating conditions studied.

Parameter	Range
Ω (rad/s)	0.33π–3.33π
N (rps)	0.25–1.67
Re (–)	2500–25 043
Fr (–)	0.02–1.07
s (–)	-1

with a ball bearing, mounted on each cylinder endwall (top and bottom). The laser plane was adjustable to visualize different cross sections, either vertical or horizontal. Table I provides a summary of the range of conditions that were investigated.

Two-dimensional, two-component (2D-2C) time-resolved particle image velocimetry (PIV) was conducted in the vertical cross section, which bisects the cylinder, and in two horizontal planes at 2 mm ($z/R = 0.04$) and 18 mm ($z/R = 0.37$) above the base of the cylinder. Neutrally buoyant non-fluorescent polyamide seeding particles (Dantec Dynamics) with a mean diameter of 5 μm were utilized as tracer particles. The temporal resolution was varied depending on the Reynolds number and the plane studied, ranging from 250 μs for the vertical plane measurements at $Re = 17530$ to 3 ms for the horizontal plane measurements at $Re = 2500$. The images were processed with an adaptive correlation processing algorithm including a 50% cell overlap and a final spatial resolution of 8×8 pixels, which was 0.28 mm in the vertical cross section (pixel size $= 3.5 \times 10^{-5}$ m) and 0.64 mm in the horizontal plane at $z = 18$ mm (pixel size $= 8 \times 10^{-5}$ m). For measurements in the vertical cross section, the field of view was $r/R = 0$–0.5, $z/R = 0$–0.5, and for horizontal ones, it was $r/R = -0.1$–1, $\theta = -100°$–$100°$, where a cylindrical coordinate system (r, θ, z) with origin at the center of the endwell is considered (see Fig. 1).

Planar laser-induced fluorescence (PLIF) was employed in the vertical midplane and in one horizontal plane at $z = 2$ mm ($z/R = 0.04$). The field of view was $r/R = 0$–1, $z/R = 0$–0.5 and $r/R = -0.1$–1, $\theta = -100°$–$100°$ for the vertical and horizontal plane measurements, respectively. This technique was used to visualize the flow during the entire duration of spin-over, from SBR in one direction to SBR in the opposite direction. For both experiments in the vertical and in the horizontal plane, a 50 μl drop of 0.5 mM solution of rhodamine 6G (Sigma) in ultrapure water was injected at the center of the endwell prior to the start of rotation. The fluid was then allowed to spin-up to solid body rotation (for approximately 5 min) before the direction of rotation was impulsively reversed. The temporal resolution for different Re and planes varied from 10 ms (100 fps) to 25 ms (40 fps), and the spatial resolution was between 4.2×10^{-5} and 8×10^{-5} m/px.

The maximum magnitude of the angular deceleration during the rotation reversal that could be achieved with the current experimental apparatus is $\pm 100\pi$ rad/s^2. The longest time taken to reverse the cylinder rotation (from $\Omega = 3.33\pi$ rad/s to $\Omega = -3.33\pi$ rad/s, i.e., $Re = 25043$) is thus 0.067 s, which can be considered instantaneous for all practical purposes. The error made in timing the inversion of cylinder rotation was approximately 5 frames or 4–15 ms, higher for lower Re, which is negligible in the context of the characteristic flow timescales, which are two-three orders of magnitude higher. To assess the error in the experimental velocity measurements, the radial profile of

the tangential velocity component at steady state, i.e., solid body rotation, was obtained from more than 7000 points across the horizontal cross section. The experimental profile was compared to the theoretical one ($u_\theta = \Omega r$), and a deviation of $\approx 0.05 \Omega R$ across the reference solid body rotation line was registered for all the configurations investigated. Experiments were carefully carried out to ensure that there was no free surface contamination.

B. Numerical modeling

The governing equation for this system is the continuity equation

$$\frac{\partial \rho}{\partial t} + \mathbf{\nabla} \cdot (\rho \boldsymbol{u}) = 0 \tag{6}$$

and the momentum equation

$$\frac{\partial (\rho \boldsymbol{u})}{\partial t} + \mathbf{\nabla} \cdot (\rho \boldsymbol{u} \boldsymbol{u}) = -\mathbf{\nabla} p + \mathbf{\nabla} \cdot \boldsymbol{\tau} + \rho \boldsymbol{g} + f_\sigma, \tag{7}$$

where $\boldsymbol{g}$ is the acceleration due to gravity, $\boldsymbol{\tau}$ is the Newtonian viscous stress tensor and f_σ is the forcing due to surface tension which is proportional to the surface tension coefficient, γ and the local curvature of the free surface.[50]

Direct numerical simulations (DNS) of (6) and (7) were carried out with the open-source computational fluid dynamics toolbox OpenFOAM using a finite volume method.[51] Three-dimensional structured meshes were generated in blockMesh. The solver used was interIsoFoam with no turbulence modeling which is appropriate for the relatively low Reynolds number considered in this simulation. A volume of fluid (VOF) method was used to treat the movement of the free surface.[52] Here, the fraction function α tracks the species in the control volume with $\alpha = 0$ and $\alpha = 1$ being a control volume that only contains either air or water, respectively. The free surface then is where $0 < \alpha < 1$. The advection equation for α is given by

$$\frac{\partial \alpha}{\partial t} + \mathbf{\nabla} \cdot (\alpha \boldsymbol{u}) = 0, \tag{8}$$

where an isoadvector scheme is used to keep the free surface sharp.[53] All schemes were second order accurate; the Crank–Nicolson scheme was used for the time integration (with a blending coefficient of 0.7), the Gauss linearUpwind numerical scheme is used for the divergence operators for the velocity field; the Gauss linear corrected numerical scheme is used for the diffusive terms while for the Gauss vanLeer scheme is used for calculating the convective term of the advection equation for α. The choice of numerical schemes is consistent with that in the literature.[50] Validation of the numerical modeling was carried out by direct comparison with the experimental data, which will be detailed in Sec. III. A mesh independence study was carried out and doubling the mesh resolution in the azimuthal, radial, and vertical directions resulted in a variation of less than 2% in the velocity profiles in the endwall and sidewall boundary layers.

The initial free surface shape at solid body rotation is given by

$$z_r = L - \frac{\Omega^2}{4g}(R^2 - 2r^2), \tag{9}$$

where z_r is the vertical position of the free surface at radius r.

In this work a cylindrical coordinate system (r, θ, z) is mostly used while a Cartesian coordinate system (x, y, z), is adopted to show contour maps of the horizontal planes, as well as to show multiple vertical cross sections extracted from the CFD data (C). In both systems, the origin is at the center of the bottom endwall. The components of the velocity vector (u_r, u_θ, u_z), defined in the cylindrical coordinate system at the initial state of solid body rotation, $t = 0$, are

$$u_r = 0; \quad u_\theta = \Omega r; \quad u_z = 0, \tag{10}$$

and at the final state of solid body rotation, $t \to \infty$, are

$$u_r = 0; \quad u_\theta = -\Omega r; \quad u_z = 0. \tag{11}$$

A reference operating condition of $Re = 3756$, corresponding to a change of rotation from $\Omega = \pi/2$ to $\Omega = -\pi/2$ rad/s, has been analyzed and discussed in detail, as it features the main flow phenomena identified during spin-over in a partially filled, which were observed for the range of Re tested. This condition was analyzed both experimentally and numerically.

III. RESULTS AND DISCUSSION

The study is structured into three subsections, focusing into different regions of the flow. First, the core flow is addressed in Sec. III A for the reference condition. The tangential velocity component at a vertical height away from both the endwall boundary layer and the free surface is analyzed (at $z/L = 0.72$, $z/R = 0.37$), and the results are compared to the classical cases of spin-up from rest and spin-down to rest. In Sec. III B, the present study focuses on the endwall boundary layer during spin-over for $Re = 3756$. The effects of varying Re are discussed afterward, in Sec. III B 3. Finally, Sec. III C focuses on the sidewall boundary layer and the generation of Taylor–Görtler (T–G) vortices during spin-over, where computational and experimental results for different Re are discussed in comparison to spin-down to rest.

A. Core flow

The tangential component of the velocity was obtained from PIV measurements in the horizontal plane at an elevation, $z = 18$ mm ($z/L = 0.72$, $z/R = 0.37$), away from both the endwall boundary layer and the free surface. Radial profiles of the instantaneous tangential velocity are presented in Fig. 2 for different instants in time, Ωt, normalized with the rotation rate of the wall at SBR for the reference condition ($Re = 3756$ and $Fr = 0.02$). The two dashed lines indicate the tangential velocity at solid body rotation at the beginning, $u_\theta(t = 0) = \Omega r$, and at the end, $u_\theta(t = \infty) = -\Omega r$, of spin-over. Figures 2(a) and 2(b) show experimental results, whereas Fig. 2(c) compares experimental and computational data. Each experimental profile [i.e., Figures 2(a) and 2(b)] comprises of more than 7000 data points across the cross section. In Fig. 2(a), the velocity profiles are smoothed with a moving average of 20 points to illustrate the stages of the spin-over process more clearly. In Fig. 2(b), the raw experimental data without any smoothing is plotted for some of the profiles in Fig. 2(a) to show the real variation of the tangential velocity with radial distance at a given instant in time. In Fig. 2(c), 2D and 3D computational data are compared to two of the raw experimental profiles in Fig. 2(b).

Initially, as seen in Fig. 2(a) at $\Omega t = 1.3$, only fluid close to the wall ($r/R > 0.9$) is affected by the change of rotation, while fluid in the core remains in solid body rotation with the original angular velocity, similarly to spin-down (see Ref. 22). Within half a revolution after
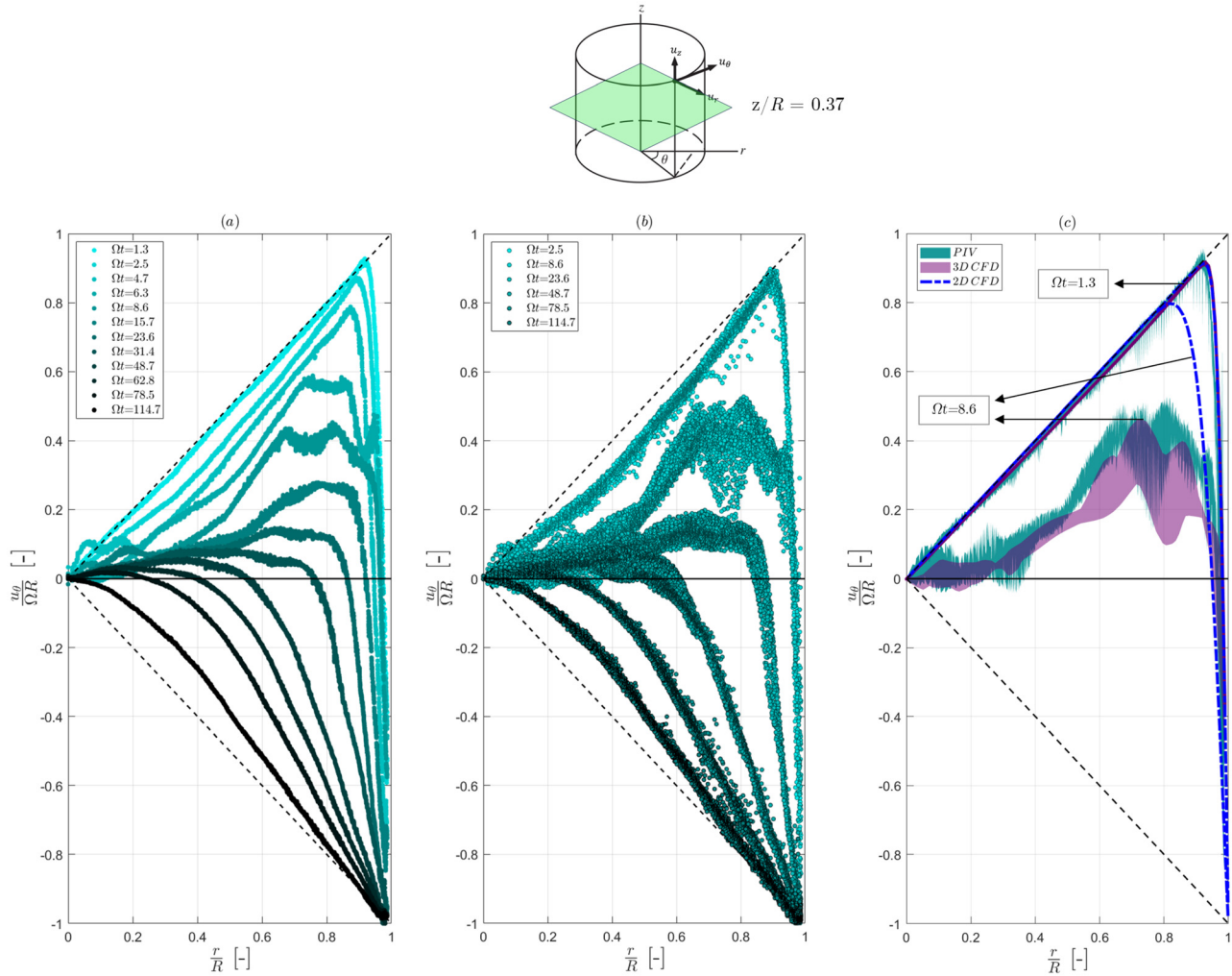
FIG. 2. Radial profiles of the instantaneous tangential velocity component at $z/R = 0.37$, for different number of revolutions after the reversal of rotation ($Re = 3756$, $Fr = 0.02$); (a) smoothed experimental profiles obtained with PIV; (b) non-smoothed (i.e., raw) experimental profiles for selected time instants in (a); (c) comparison of experimental (cyan) and computational (magenta) results at an early instant, $\Omega t = 1.3$, and a later instant, $\Omega t = 8.6$; the shaded regions represent the variation in the tangential component at a given radius; the dashed curves show the two-dimensional numerical solution.

the change of rotation, at $\Omega t = 2.5$, fluid in the core has already lost angular momentum and is no longer rotating as a solid body, but instead it is characterized by regions with varying local angular velocity, $\omega = \frac{\partial u_\theta}{\partial r}$. This is in agreement with the work of Stewartson et al.[43] and is in sharp contrast with the mechanics of spin-down to rest, during which fluid in the core keeps rotating rigidly with decaying angular velocity.

Between $2.5 \leq \Omega t \leq 8.6$, the shape of the peak of each profile is affected by the onset of turbulence in the sidewall boundary layer due to the emergence of Taylor–Görtler vortices. This effect is better visualized in Fig. 2(b), where the raw experimental data are shown for all 7000 points in the cross section without any smoothing, revealing the actual variance of u_θ at a given radius. In the early moments, i.e., Fig. 2(b), $\Omega t = 2.5$, the profiles are relatively smooth, indicating little variation in the tangential velocity across the entire plane at any given

radial coordinate. However, after the onset of the Taylor–Görtler vortices at $\Omega t = 4.2$ (discussed later in Sec. III C), fluid in the sidewall boundary layer transitions to turbulence, breaking the axisymmetry of the flow and resulting in a significantly broader scatter of the data points observed at $\Omega t = 8.6$. As the turbulence decays, the variability of the tangential velocity at a given radius decreases, and in the late stages ($\Omega t > 48.7$), the profiles once again become smooth and narrowly scattered.

As more fluid near the sidewall is spun up in the new (negative) direction [Figures 2(a) and 2(b)], the thickness of the sidewall boundary layer, indicated by the border between positively and negatively rotating fluid, increases as that border moves radially inward. Meanwhile, fluid in the interior continues to lose angular momentum in the original (positive) direction. Consequently, the spin-over process can be viewed as a combination of spin-up and spin-down occurring

simultaneously. After a critical point in time (i.e., $\Omega t = 78.5$), rotation in the original direction has completely decayed, and the profiles are characterized by a negative tangential velocity close to the wall, while in the interior $u_\theta \approx 0$. From that point onward, the spin-over process becomes entirely spin-up until the fluid is again in solid body rotation in the new direction.

In Fig. 2(c), three-dimensional DNS results (magenta) are plotted against the raw experimental data (cyan) from Fig. 2(b) for an early instant in time, $\Omega t = 1.3$ while the fluid in the core is still in solid body rotation, and a later instant in time, $\Omega t = 8.6$, after the onset of three-dimensional turbulence in the sidewall boundary layer due to the T–G vortices. In addition, 2D numerical results (for a horizontal plane in an infinite cylinder) are also included as dark blue dashed curves for both instants in time. The 3D CFD data were obtained from four radial profiles 90° apart, extracted from the horizontal cross section. The variation of the instantaneous tangential velocity, u_θ, at a given radial coordinate is represented as a shaded region (CFD in magenta, PIV in cyan).

In Fig. 2(c), very good agreement is observed between the experimental and the 3D computational data at each instant. At the early instant ($\Omega t = 1.3$), the flow is symmetric around the axis of rotation, but at the later instant ($\Omega t = 8.6$), the symmetry is broken and variation is observed in the tangential component of the velocity at a given radial distance. The radial range and extent of CFD variation, illustrated by the region shaded in magenta, overlaps significantly with that of the experimental data, represented in cyan. This good agreement demonstrates that the three-dimensional solution can fully capture the chaotic nature of the flow. The 2D numerical solution, on the other hand, shows good agreement at the first instant but fails to accurately predict the tangential velocity decay at the later instant. This discrepancy is due to the absence of the endwall boundary layer in the 2D model, which is critical for driving the faster decay of rotation through convection.

In order to separate the decay of rotation in the original direction from the gain of rotation in the new direction, the instantaneous experimental profile of the tangential velocity component in each instant in time was divided into a positive and negative part, and the corresponding integral with respect to the radial coordinate was taken, thus yielding the instantaneous positive, Φ_θ^+, and negative, Φ_θ^+, planar tangential fluxes,

$$\Phi_\theta^+ = \int_0^R \frac{u_\theta^+}{\Omega R^2}\, dr, \tag{12}$$

$$\Phi_\theta^- = \int_0^R \frac{u_\theta^-}{\Omega R^2}\, dr, \tag{13}$$

with u_θ^+ being equal to the positive part of the velocity profile (i.e., $u_\theta^+ = u_\theta$ for $u_\theta > 0$) and 0 when it is negative (i.e., $u_\theta^+ = 0$ for $u_\theta < 0$), and u_θ^- being equal to the negative part of the profile (i.e., $u_\theta^- = u_\theta$ for $u_\theta < 0$) and 0 when it is positive ($u_\theta^- = 0$ for $u_\theta > 0$). The positive, Φ_θ^+ (magenta), and absolute value of the negative, Φ_θ^- (cyan), tangential fluxes at $z/R = 0.37$ are plotted against Ekman time, T, in Fig. 3 for $Re = 3756$, 7513, $17\,530$, and $25\,043$. The color darkens with increasing Re. As a reference, the solid black curve indicates the decay of tangential flux during spin-down (SD) to rest from solid body rotation, while the dashed curve with shaded area around it shows the gain of tangential flux during spin-up (SU) from rest. It is
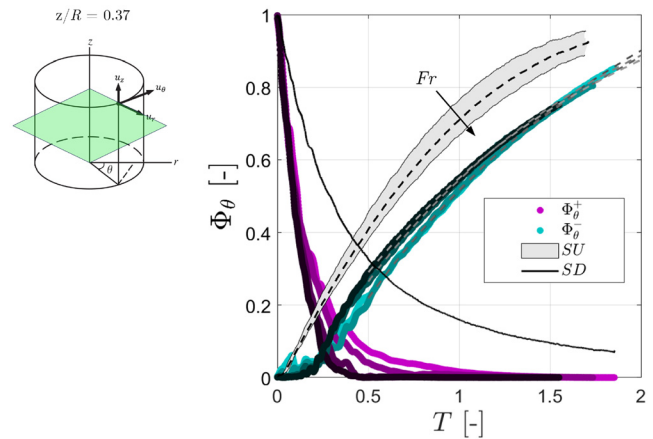

FIG. 3. Decay of positive planar tangential flux, Φ_θ^+, (magenta) and gain in (absolute value of the) negative planar tangential flux, Φ_θ^-, (cyan) at $z/R = 0.37$ during spin-over for $Re = 3756$, 7513, $17\,530$, and $25\,043$ ($Fr = 0.02$–1.07); the shade of color is darker for higher Re; the solid black curve indicates the decay of tangential flux for spin-down to rest across the range of Re and Fr; the dashed curve and shaded gray area around it illustrate the gain of tangential flux during spin-up from rest for the range of Re and Fr.

worth to remark that the spin-down process is completely scalable with Re, and therefore, a single curve is used to represent the process for the range of Reynolds and Froude numbers considered here. On the other hand, for spin up the Ekman timescale becomes progressively longer with increasing Fr (and therefore Re) due to the deformation of the free surface (see Ref. 22). The shaded region surrounding the dashed curve captures this variability with Re and Fr.

At $T = 0$, the fluid is in solid body rotation, and the normalized tangential flux in the original direction is 1, while that in the new (negative) direction is 0. In the early stages of the process ($T < 0.2$), rotation in the original direction is seen to decay at a very fast rate, while at the same time the negative tangential flux remains close to 0. This leads to the fluid losing most of its tangential flux in the old direction before it begins gaining it anew in the opposite direction. The minimum absolute tangential flux reached in the system is at the intersection of the two curves and moves to lower minimum values, occurring at earlier Ekman times with increasing Re. For example, at $Re = 3756$, the minimum absolute tangential flux is 0.29 and occurs at $T = 0.36$, while for $Re = 25\,043$, it is 0.15 and occurs at $T = 0.25$. Compared to spin-down to rest (solid black curve), the loss of angular momentum occurs at a much faster rate during spin-over. To put in perspective the positive tangential flux decays to below 5% of the original value at $T = 0.26$–0.63 for the range of Re considered (sooner for higher Re), while for spin-down the corresponding Ekman time was found to be $T = 2.68$.[22]

When the negative flux is considered, i.e., the gain of momentum in the new direction, an initial lag up to $T \approx 0.2$ is present, as mentioned earlier, which does not occur in the corresponding spin up curve, characterized by a nearly linear increase in the first instants of the process. The gain of tangential flux during spin-up from rest is initially faster than spin-over because spin-up benefits from the Ekman pumping mechanism, which through convection, puts fluid in rotation, whereas this mechanism is absent in the early stages of spin-over

and the fluid gains momentum in the new direction through viscous diffusion. After the initial lag, however, the shape of curve is similar to that of spin-up, indicating a resemblance in the fluid mechanics between late-stage spin-over and spin-up.

Wedemeyer's analytical model for spin-up in a completely filled cylinder[12] shows that the Ekman pumping mechanism of the endwall boundary layer generates a cylindrical shear front of tangential velocity, which propagates radially inward from the sidewall to the axis of rotation in a predictable manner. As discussed in Sec. I, the radial position of the shear front in Ekman time is used as a parameter to establish the timescale of the spin-up process. This follows an exponential decay law in Ekman time,

$$\frac{r^\star}{R} = ae^{-\frac{T}{T_d}}, \tag{14}$$

where $r^\star$ is the radial position of the propagating front. For spin-up from rest, $a = 1$. Similarly to spin-up from rest, geostrophic flow is also established in the later stages of spin-over. In order to compare the timescales of the two processes, the position of the propagating vertical shear front was obtained from the tangential velocity profiles at $z/R = 0.37$ for spin-over in the same way as it was for spin-up.[22] The radius at which the tangential velocity reaches 5% of the new velocity of the wall was found, i.e., $u_\theta/\Omega R = 0.05$ for spin-up and -0.05 for spin-over. The results are shown in Fig. 4.

The radial position of the propagating shear front is shown with magenta-cyan lines for spin-over, and with a dashed curve surrounded by a shaded gray region for spin-up. The magenta part of each spin-over curve indicates the period of decay of tangential flux in the original direction of rotation, as found in Fig. 3, after which the fluid enters the spin-up phase (cyan part). The color darkens for increasing Re, analogously to Fig. 3. The black dashed curves show the exponential fit to the spin-over data, discussed below. Each process is considered
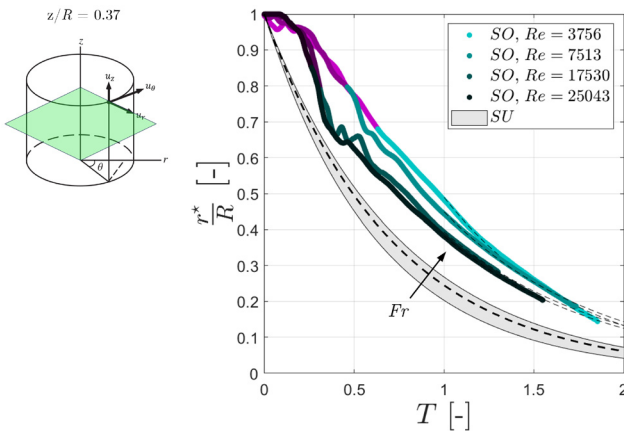
FIG. 4. Radial position, $r^\star$, of the propagating vertical shear front of the tangential velocity observed during spin-over (colored curves) and spin-up from rest (dashed black curve and gray band around it, representing the variation within the range of Re), obtained from PIV measurements in the horizontal plane at $z/R = 0.37$ for $Re = 3756$–25 043, $Fr = 0.02$–1.07. The magenta part of each spin-over curve indicates the period of decay of rotation in the original direction, while the cyan part indicates the period of gain of rotation in the new direction (as found from Fig. 3). The color darkens with increasing Re. The dashed gray curves indicate the exponential fit to each cyan curve.

complete when the front has propagated inward 95% of the cylinder radius, i.e., to a radial coordinate of $r^\star/R = 0.05$.

Each spin-over curve appears to be made up of two parts: an early convex region, when the fluid is mainly losing angular momentum, and a concave region, when it is gaining momentum in the new direction. The inflexion point is around the time when rotation in the original direction has decayed (end of magenta and beginning of cyan), indicating a transition to the spin-up stage, where the Ekman pumping mechanism dominates the flow and drives the propagation of the shear front. In order to compare with the front propagation during spin up, an exponential decay was fit to the spin-over results, according to Eq. (9). The curve was fit through the data for $T \geq 1$, since in the beginning, the spin-over process is mainly spin-down, and while there is a shear front between the positively and negatively rotating fluid, it is still not propagating as the Ekman pumping is not yet established, and instead the front is diffusing inward. The exponential fit to each dataset is represented by the thin dashed gray curves in Fig. 4. The Ekman decay timescale, T_d, are reported in Table II, alongside analogous values for spin-up from rest.[22]

In agreement with spin up, an increase in the Ekman decay timescale, T_d, is observed with increasing Re. This is the increasing impact of the free surface deformation (increasing Froude number), which slows the spin-up process down, and is consistent with previous findings for linear spin-up in a partially filled cylinder.[20,21] A comparison between spin-up and spin-over reveals that the front propagates more slowly during spin-over, indicated by the longer characteristic Ekman decay timescale, T_d). The reason for this may be modification to the Ekman pumping since the state of the fluid at the beginning of the spin-up phase of spin-over is not complete rest, as it is for spin-up.

While both spin-up and spin-down are individually faster than spin-over for the case of interest considered, spin-over still occurs on the (convective) Ekman timescale, which can be expected since it is predominantly (in time) a spin-up process.

B. Endwall boundary layer

This section focuses on the endwall boundary layer during spin-over, how it drives convection in the interior and leads the fluid to transition from spin-down to spin-up. The action of the boundary layer is examined in detail for the reference condition, $Re = 3756$, $Fr = 0.02$, during the early (Sec. Sec. III B 1) and late (Sec. III B 2) stages of spin-over. Experimental and computational data are presented to

TABLE II. Characteristic spin-up (SU) and spin-over (SO) Ekman decay timescales for different Re and Fr.

N (rps)	Re (−)	Fr (−)	Mode	T_d (−)
0.25	3756	0.02	SO:	0.76
			SU:	0.63
0.50	7513	0.10	SO:	0.87
			SU:	0.69
1.17	17 530	0.53	SO:	0.92
			SU:	0.77
1.67	25 043	1.07	SO:	0.89
			SU:	0.76

characterize the different flow stages in both horizontal and vertical cross sections.

1. Early stages

Figure 5 shows PIV and CFD data obtained from the horizontal plane at an elevation, $z = 2$ mm ($z/R = 0.04$), for different instants during the first half of a revolution after the reversal of rotation. Plots in each row show the same instant in time. The left and middle columns illustrate a contour plot of the experimental tangential and radial velocity components, respectively. The third column shows the tangential (magenta) and radial (cyan) velocity profiles along the radius. The markers indicate experimental data, while computational results are represented with solid curves. Similarly to Fig. 2, the dashed lines show the tangential velocity profiles at solid body rotation at the start and at the end of spin-over.

Computational results are in very good agreement with the experiments during the early stages of spin-over ($\Omega t = 0.31$–3.14). In the first instant considered after the reversal of rotation, $\Omega t = 0.31$ (first row in Fig. 5), a thin boundary layer develops along the cylinder wall, where viscous diffusion is dominant and the fluid decelerates and accelerates in the new direction, while the entire inner core of fluid continues to rotate rigidly with the original angular velocity at solid body rotation. At this time, the radial velocity is close to 0 (i.e., the contour map of the radial velocity component shows mainly experimental noise).

At $\Omega t = 1.26$, the tangential velocity in the inner endwall boundary layer, $r/R < 0.8$, begins to decrease rapidly. A similar observation was also made in Fig. 2 for a plane above the endwall boundary layer ($z/R = 0.37$), at a slightly later instant in time ($\Omega t = 2.5$). From the radial velocity contour plot at $\Omega t = 1.26$, it is seen that the endwall boundary layer becomes of the Bödewadt type, characterized by a strong radial inflow, $u_r < 0$ (complemented by an axial efflux out of the plane, which is not shown here). The maximum magnitude of (inward) radial velocity occurs at $r/R \approx 0.65$.

At $\Omega t = 1.88$ (third row), rotation in the center at $r/R < 0.3$ has decayed to ≈ 0, while fluid in the outer region, approximately $0.6 < r/R < 0.8$, appears to have restored some of its rotation (in the original direction), and locally the profile once again matches that at initial SBR. At the same time the negative radial velocity keeps decreasing in the inner region, $r/R < 0.5$, and reaches a magnitude comparable to the local tangential component at the endwell. The radial velocity profile peak has also shifted radially inward to $r/R \approx 0.5$, indicating the existence of a propagating radial wave, which speeds up as it contracts. In the next instant, $\Omega t = 2.20$, the radial wave has propagated further radially inward to $r/R = 0.46$, and fluid on the inside of the circular wave, $r/R < 0.43$, begins gaining tangential velocity in the new direction of rotation (i.e., clockwise).

By $\Omega t = 2.67$, the counter-rotating region ahead of the wave has contracted to $r/R < 0.38$ and has reached the angular velocity of the endwall, while the wave peak of the radial velocity profile, seen at $r/R = 0.39$, is much sharper. It is worth noting that at this instant, the fluid immediately behind the radial wave, at $r/R = 0.4$, rotates (in the original direction, anticlockwise) with an angular velocity marginally exceeding that at SBR. A similar phenomenon was described on the transient flow between two parallel disks in a fluid at rest, which are impulsively set in rotation in opposite directions.[45] Also in this study the flow exhibited velocity magnitude greater than the rotating disks.
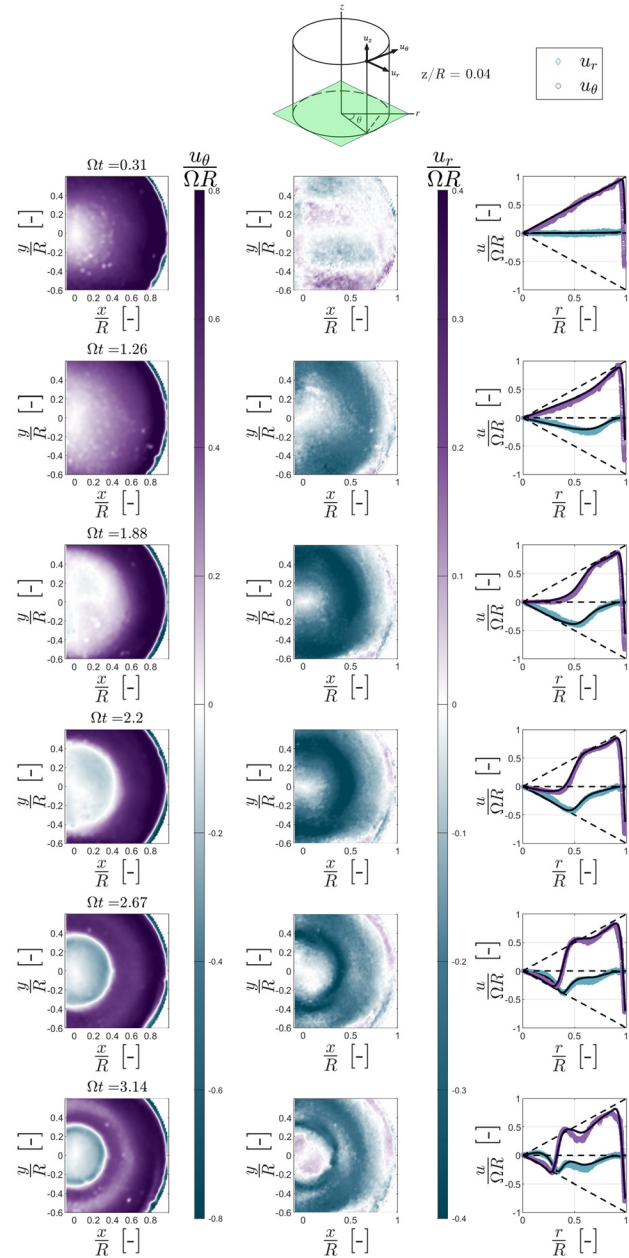

FIG. 5. PIV contour plots of the instantaneous tangential (left) and radial (middle column) velocity component in the endwall boundary layer ($z/R = 0.04$) for $Re = 3756$, $Fr = 0.02$, at different instants after the reversal of cylinder rotation; the third column shows the corresponding profiles of the tangential (magenta) and radial (cyan) velocity components along the radius. Experimental data are plotted with markers, while CFD data are illustrated with solid curves. The dashed lines show the tangential velocity profile at solid body rotation in each direction.

At $\Omega t = 2.67$, it is also seen that the profile of the radial velocity is characterized by a second, smaller negative peak further radially out at $r/R = 0.68$, indicating the formation of a second circular radial wave. Similarly to the first wave, the appearance of the second wave is also

characterized by a local minimum in the tangential velocity component at $r/R = 0.63$, present in both computational and experimental data, where fluid ahead of the second radial wave is losing angular momentum.

In the final instant shown, $\Omega t = 3.14$, the second radial wave is seen more clearly, and it has propagated radially inward to approximately $r/R = 0.58$. At that time, fluid immediately in front and behind the first radial wave (which is now at $r/R = 0.28$) is seen to exceed the angular velocity of the wall, in the negative (new) and in the positive (old) direction, respectively, while the radial velocity component, in the inner counter-rotating region, is seen to change sign, at $R_{s1} = r_{s1}/R = 0.22$. This point is here referred to as "stagnation point," but it only relates to the radial velocity being zero. From this instant onward two distinct and opposing flow regions can be identified: an inner endwall boundary layer ($r/R < R_{s1}$) of the von Kármán type, where fluid rotates with the new angular velocity of the wall and is pumped radially outward, and the outer endwall boundary layer ($r/R > R_{s1}$) of the Bödewadt type, still characterized by a strong radial inflow and rotation in the original direction.

The formation of a stagnation point in the endwall boundary layer agrees with similar spin-over studies available for different configurations,[43,47,49] where the latter two studies addressed time-independent problems.[47,49] Stewartson et al.[43] studied analytically the transient flow induced by an steadily rotating finite disk, which is impulsively reversed, and showed that at $\Omega t = 2.359$ a singularity forms in the boundary layer. The experimental data presented in Fig. 5 exhibits the first formation of the "stagnation point" in the boundary layer slightly later in time, between $2.67 < \Omega < 3.14$. This can be explained by considering that PIV measurements were taken slightly above the endwall ($z/R = 0.04$), and some additional time is necessary for the radial velocity stagnation point formed at the endwall and its associated flow perturbations to manifest at the experimental horizontal plane ($z/R = 0.04$). This is further confirmed by analogous data extracted from the CFD simulations at a lower plane, $z/R = 0.01$, which exhibited the "stagnation point" forming at the same radial location as at $z/R = 0.04$, i.e., $R_{s1} = 0.22$, but earlier in time than in the experiment ($z/R = 0.04$), at $\Omega t = 2.36$, in remarkable agreement with the onset of the singularity reported by Stewartson et al.[43]

To gain more insight into the transient phenomena described in Fig. 5, further analysis is carried out on the flow in the vertical midplane. Figure 6 illustrates PLIF data alongside CFD data at different number of revolutions after the reversal of rotation for the reference condition, $Re = 3756$ and $Fr = 0.02$. Data in each row illustrates the tangential, radial and axial components of the velocity in the plane from left to right, while the last column shows PLIF experiment at corresponding instant in time. The PLIF colormap shows the normalized pixel brightness, C, where at the moment of injection, the drop of dye has a normalized brightness of $C = 1$, while the remainder of the fluid has a normalized brightness, $C = 0$. As a reference, the position of the lowest PIV plane, $z/R = 0.04$, examined in Fig. 5, is illustrated with a horizontal black dashed line. The vertical dashed line, where included, indicates the instantaneous radial location of the stagnation point, R_{s1}, found from the CFD data in close proximity to the bottom, $z/R = 0.01$.

The first instant shown in Fig. 6, $\Omega t = 1.26$, illustrates the establishment of the Bödewadt-type boundary as discussed in Fig. 5, characterized by a strong radial inflow, as seen in the contour plot of the

radial velocity. At this time, the endwall boundary layer height is relatively uniform with a thickness of $\delta_E = 0.07$. This was estimated from the average distance from the bottom, z/R, at which the axial profile of the radial velocity component is equal to 0.

The second instant in Fig. 6, $\Omega t = 2.36$, is when the stagnation point is first observed in the boundary layer and the flow no longer resembles that during spin-down. In agreement with the data in Fig. 5, a thin region exists near the center of the bottom, where the fluid is rotating in the new (negative) direction of rotation, opposite to the bulk flow. Within that same region, the radial component of the velocity is also reversed, and a stagnation point is observed at $R_{s1} = 0.22$, indicated by the vertical dashed line in Fig. 6. At $\Omega t = 2.36$ is also seen that the boundary layer has significantly thickened near the axis of rotation, where it reaches a maximum thickness, $\delta_E = 0.14$, at $r/R \approx 0.1$, nearly double that in the previous instant shown. In the tangential velocity contour plot (first column), a thin layer near the endwell is visualized in cyan, where fluid is rotating in the new direction, at $r/R < 0.5$. The axial velocity contour map in Fig. 6 shows an intensified axial outflow from the boundary layer, right above the counter-rotating region, where the boundary layer is thickest. This is in agreement with the PLIF contour map at this instant, where dye, pushed radially inward along the bottom, is lifted away from the endwall and passes above the counter-rotating region point as it continues to travel radially inward. At this time, the development of a single vortex at the free surface, preceding the Taylor–Görtler instabilities is also observed near the sidewall (top right corner) in the CFD contour plots, which is not visualized in this particular PLIF experiment due to the absence of fluorescent dye in that region.

By $\Omega t = 3.14$ in Fig. 6, the counter-rotating region near the center of the bottom has expanded both radially to $r/R = 0.25$ (vertical dashed line) and vertically to $z/R = 0.1$, and represents a small core of fluid, where all three velocity components are in the opposite direction with respect to the bulk flow, established in the previous instances shown. Within this inner core of fluid, the direction of circulation is consistent with that during spin-up in a cylinder, generated by the endwall boundary layer which is of the von Kármán type (Ekman layer). For this reason, the inner core of fluid with opposing circulation, observed at $\Omega t = 3.14$, is hereafter referred to as the "von Kármán bubble" because originated in the von Kármán boundary layer. It is visualized by the streamlines in the bottom left corner of each contour plot, where the fluid is circulating axially down and radially out, as it is spinning in the new direction of rotation. The "von Kármán bubble" visualized through the computational data, is also in very good agreement with the corresponding experimental PLIF image at $\Omega t = 3.14$, where some of the dye transported inward by the boundary layer becomes entrained in the "von Kármán bubble," and its path curls downward and then radially outward, forming a small anti-clockwise loop. Due to the continued expansion of the "bubble" at the center of the bottom, the interior flow is altered and the streamlines now form multiple smaller closed flow cells in the interior. In contrast, during spin-down, the (Ekman-like) convection generated is one-directional, i.e., the streamlines in the interior form a single large loop (similarly to the first instant shown in Fig. 6).

In the final instant shown in Fig. 6, $\Omega t = 4.24$, the "von Kármán bubble" has detached from the endwall and can be seen "floating" in the interior along the axis of rotation, at approximately halfway toward the free surface. A stagnation radius still exists on the endwall, where
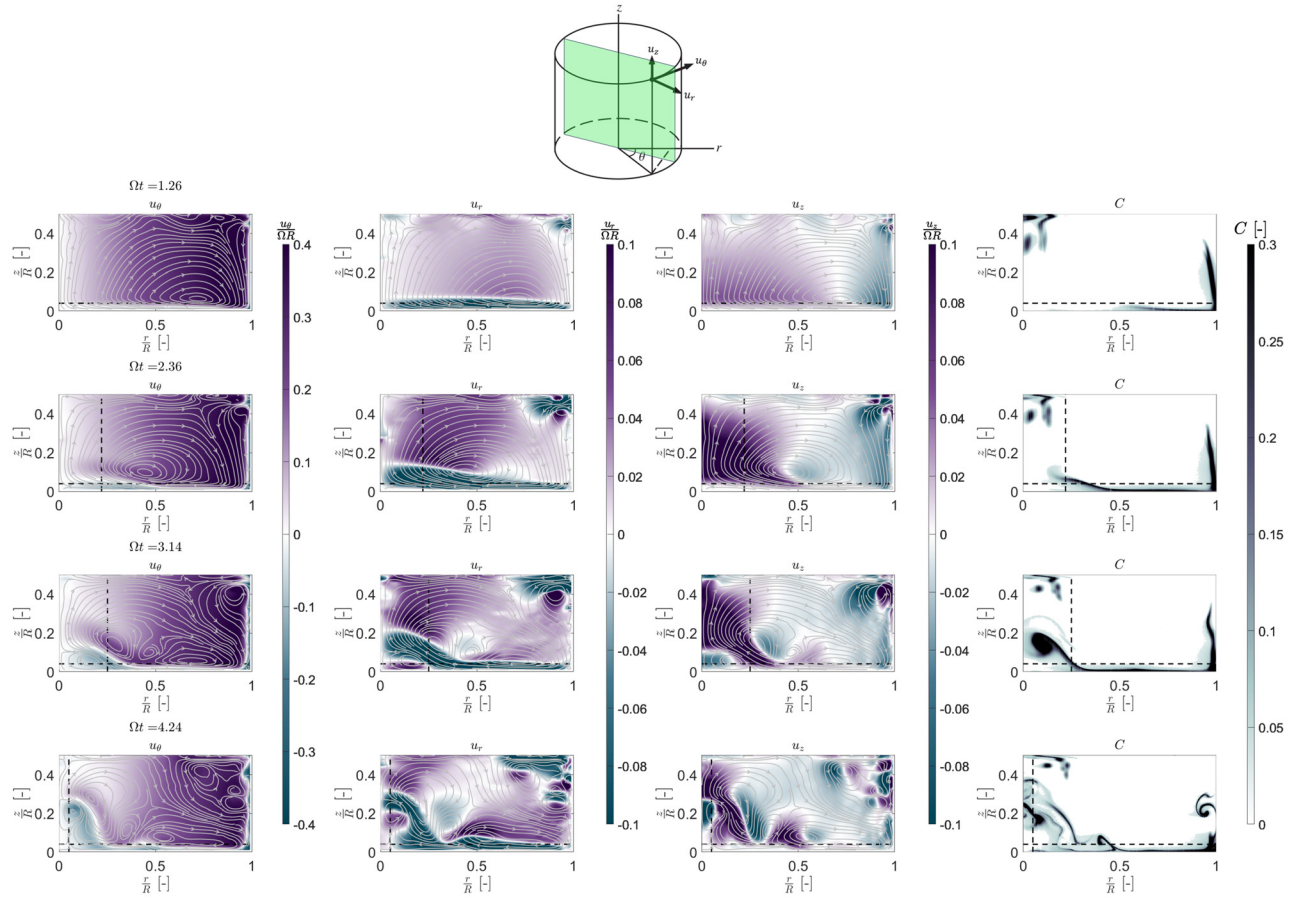
FIG. 6. CFD contour plots of the instantaneous velocity components in the tangential, radial and axial direction, u_θ, u_r, and u_z (columns left to right), and the corresponding PLIF image (fourth column) in the vertical midplane at different number of revolutions after the reversal of rotation, $\Omega t = 1.26$–4.24 for $Re = 3756$, $Fr = 0.02$; the horizontal dashed line in each image indicates the vertical position of the horizontal PIV measurement plane in the endwall boundary layer at $z/R = 0.04$; the vertical dashed line at $\Omega t = 2.36$–4.24 indicates the instantaneous radial location of the stagnation point.

the radial flow direction is reversed, but it is significantly closer to the axis of rotation, at $r/R = 0.05$ (vertical dashed line). The division of the flow into multiple smaller cells with closed streamlines is strengthened, and two main circulation paths can be identified through the endwall boundary layer. Instead of one large convection loop, as seen in spin-down, the interior fluid domain during spin-over is recirculated via two separate routes based on the distance of fluid from the axis of rotation. Approximately fluid within the inner half of the radius ($r/R \leq 0.5$) is pulled axially down into the endwall boundary layer at $r/R \approx 0.3$, forming the inner convection loop. In contrast, fluid in the outer half of the radius ($r/R > 0.5$) is drawn into the endwall boundary layer near the sidewall and is expelled from it at $r/R \approx 0.5$, forming the outer convection loop. This pattern is also visualized in the PLIF image, where the dye is seen traveling upward away from the boundary layer at approximately $r/R = 0.5$. Additionally, a pair of counter-rotating Taylor–Görtler vortices is observed at the sidewall, as confirmed by both CFD and PLIF data.

To better illustrate the flow characteristics at this stage, a schematic is included in Fig. 7, based on the streamlines of Fig. 6 for two

selected instants in time: the moment the stagnation point occurs in the endwall boundary layer, $\Omega t = 2.36$ [Fig. 7(a)], and the moment the "von Kármán bubble" detaches from the endwell, $\Omega t = 4.24$ [Fig. 7(b)]. The red and blue arrows at the bottom indicate the radial velocity direction in the endwall boundary layer.

In Fig. 7(a), the stagnation point has just formed in the endwall boundary layer, and the counter-rotating fluid is in very close proximity to the bottom. The original single convection stream, illustrated with black arrows, remains unaltered and is similar to that observed during spin-down. In Fig. 7(b), the "von Kármán bubble" with opposite circulation, labeled "K," has developed and detached from the endwall boundary layer. This detachment results in the division of the original convection into inner and outer circulation loops, as discussed in Fig. 6, which are sketched in cyan and magenta, respectively. The Taylor–Görtler instabilities are labeled "TG," and the single vortex near the free surface, which forms prior to them, is denoted with "S."

A similar phenomenon to the formation of a flow region in the boundary layer with opposite circulation to the remaining fluid and the division of the flow into different closed compartments or "cells"
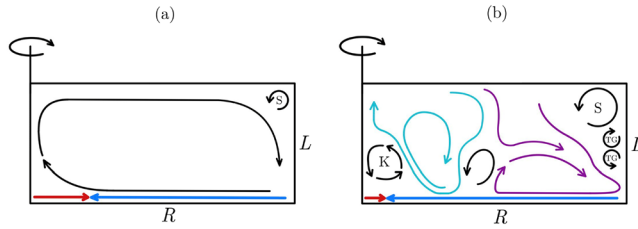
FIG. 7. Schematic representation of the flow pattern during the early stages of spin-over observed for $Re = 3756$; (a) $\Omega t = 2.36$, onset of boundary layer separation, and (b) $\Omega t = 4.24$, detachment of the "von Kármán bubble" from the endwall boundary layer. The red and blue arrows indicate the radial velocity in the boundary layer; the "von Kármán bubble" is labeled with "K," the Taylor–Görtler vortices with "TG" and the single vortex observed near the free surface with "S"; the inner and outer circulation flow cells are illustrated with cyan and magenta streamlines, respectively.

was also described for the time-independent flow in a completely filled rotating cylinder with a counter-rotating top endwall of similar aspect ratio to that discussed here ($H/R = 0.5$).[48] Provided that the counter-rotation was sufficiently strong ($s < -2.7$), they observed a free shear layer, which was seen to "flip-flop" from one endwall to the other, briefly remaining in the interior as a separate structure with opposite circulation. In the transient case with a free surface considered here, the "von Kármán bubble" detaches from the endwall due to the ongoing strong Bödewadt radial influx, and eventually dissipates as it travels upward along the axis of rotation, causing velocity fluctuations all the way at the surface, observed with both CFD and PLIF. This complex mechanism results in multiple recirculation loops, which enhance the convection of interior fluid, as well as in a region near the axis, at the interface of the "bubble," where a shear layer exists as counter- and co-rotating fluid mix. Altogether, this could explain the accelerated loss of angular momentum, occurring far from the endwall boundary layer (i.e., at $z/R = 0.37$) in the early stages of spin-over, which was reported in Sec. III A.

2. Late stages

This section focuses on the late stages of spin over, $\Omega t > 4.24$. The same (reference) condition as in Sec. III B 1 is considered, $Re = 3756$, $Fr = 0.02$. Figure 8 shows instantaneous PIV, CFD and PLIF data both in the horizontal midplane at $z/R = 0.04$ (i.e., inside the endwall boundary layer), and in the vertical cross section. The first column includes a PIV contour plot of the tangential velocity in the endwall boundary layer, accompanied by the tangential (magenta) and radial (cyan) velocity profiles in the second column. Markers indicate experimental data, while CFD profiles are shown with dashed (radial velocity) and solid (tangential velocity) lines, where available ($\Omega t \leq 5.34$). The third and fourth columns visualize the flow with PLIF experiments in the endwall boundary layer at $z/R = 0.04$, and in a vertical midplane, respectively. The horizontal dashed line in the vertical cross section represents the position of the horizontal plane at $z/R = 0.04$.

The first instant in Fig. 8, $\Omega t = 4.24$, corresponds to the detachment of the "von Kármán bubble" from the endwall. Concurrently, the second radial wave, already reported at $\Omega t = 2.67$ in Fig. 5, has propagated to approximately half of the radius, as indicated by the local minimum (negative peak) in the radial velocity profile at $\Omega t = 4.24$ in Fig. 8. At the same time, the tangential velocity at this radial location has changed sign, and the circular radial wave is visualized in the tangential velocity contour plot as a ring of fluid (cyan), spinning in the new direction. The appearance and behavior of these two concentric radial waves are similar to type II waves, characteristic of Bödewadt boundary layers, as well as the boundary layer on a counter-rotating disk.[4,47,49] The emergence of the second type II wave results in a high shear region with enhanced mixing at the interface of co- and counter-rotating fluid, visualized in the horizontal plane PLIF images at $\Omega t = 4.24$ and $\Omega t = 5.34$, where the dye is seen to form rolls.

When considering $\Omega t = 5.34$, it becomes evident from the velocity profiles that the appearance of the second type II wave results in the formation of an additional radial stagnation point at $R_{s2} = 0.4$, marked by inversed (positive) radial velocity. This occurrence triggers boundary layer separation at the same radius where the second Type II wave is seen, at $r/r \approx 0.5$, identified by (negative) tangential velocity in the new direction of rotation. This is further confirmed in the PLIF image in the vertical cross section, where the dye in the endwall boundary layer is carried vertically upward at the new stagnation point.

In Fig. 8 at $\Omega t = 9.97$, spiral waves are observed in the contour plot, characterized by inversed (negative) tangential velocity, which are similar to Type I waves. The existence of type I spiral waves, which co-rotate with the counter-rotating disk where they are formed, has also been reported by Gauthier et al. Type I waves are described as "stationary spiral vortex rolls" (Faller 1991), as they are seen to remain at roughly the same position throughout their existence ($6.28 < \Omega t < 22.00$). The spirals are also visualized in the PLIF images in either cross section at $\Omega t = 9.97$. In the horizontal plane, their appearance is similar to that in the tangential velocity contour plot and three spiral "arms" are observed in half of the cross section. The PLIF image in the vertical plane is also in agreement, where the spiral waves, bisected by the laser plane, appear as rolls/curls near the bottom, and again three rolls are seen in half of the cross section at approximately $r/R = 0.3$, 0.5, and 0.8.

At the next instant in Fig. 8, $\Omega t = 15.71$, the spiral waves, although still visible, have begun decaying along with the original (positive) rotation in the boundary layer. By $\Omega t = 22$ (not shown), these waves disappear, and the fluid enters the final phase of the spin-over process: spin-up. This stage is visualized at $\Omega t = 48.69$, where the tangential velocity is negative in the outer part of the endwall boundary layer and approximately zero in the inner part. The radial velocity profile is positive, indicating a radial outflow across the entire endwall boundary layer, now of the von Kármán type, similarly to spin-up. The sidewall boundary layer is of the Stewartson type, transporting fluid upward from the endwall boundary layer along the sidewall. This creates a vertical shear front of tangential velocity, propagating toward the axis of rotation, similarly to the spin-up process discussed in Sec. III A.

At $\Omega t = 48.69$, the front is positioned at $r^*/R = 0.6$, as obtained from Fig. 4 ($z/R = 0.37$), illustrated with a dashed circle in the horizontal plane and a dashed vertical line in the vertical plane. The contour plot of the tangential velocity component shows the fluid behind the front (radially outward) rotating in the new direction, while fluid ahead of the front (radially inward) is at rest. In the PLIF image of the bottom, dye streaks behind the front are aligned and parallel to the wall, while ahead, the dye pattern is random due to chaotic mixing during the type I and type II wave stages. In the vertical cross section PLIF image, dye on the outer side of the front forms parallel vertical
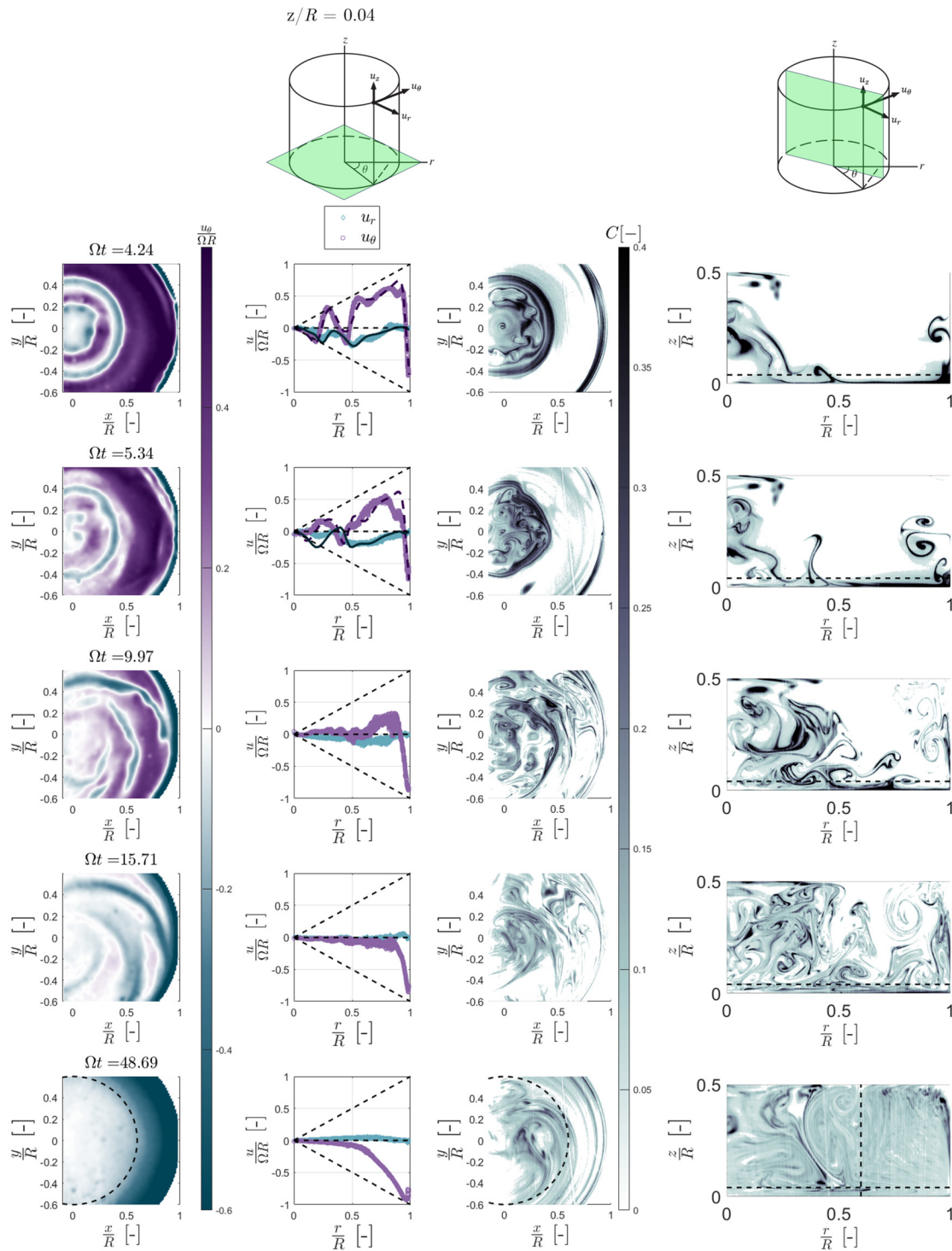
FIG. 8. First column: PIV contour plot of the instantaneous tangential velocity in the endwall boundary layer at $z/R = 0.04$; second column: radial (cyan) and tangential (magenta) velocity profiles in the endwall boundary layer from PIV (markers) and CFD (solid curves); third column: PLIF in the endwall boundary layer: fourth column: PLIF in the vertical midplane; $\Omega t = 4.24$–48.7, $Re = 3756$, $Fr = 0.02$. The horizontal dashed line in the vertical plane indicates the vertical position of the horizontal PIV plane at $z/R = 0.04$; in the last row, the dashed circle in the horizontal plane and the vertical dashed line in the vertical plane indicate the radial position of the propagating shear front of tangential velocity, also observed during spin-up.

streaks, while on the inner side, it shows a random pattern. Videos capturing these mechanisms on vertical cross sections are available for three different Reynolds numbers. These are linked to Fig. 9(d) for $Re = 3756$ (multimedia available online), Fig. 9(e) for $Re = 7513$ (multimedia available online) and Fig. 9(f) for $Re = 17\,530$ (multimedia available online). In these videos the vertical shear front can be clearly seen in the late stages of spin-over. This flow persists until the entire fluid body attains solid body rotation with the new angular velocity of the wall.

3. Trends with Re

This section focuses on the impact of varying the cylinder rotational speed ($2504 < Re < 25\,043$) on the key characteristics of the endwall boundary layer during spin-over, which so far have been described only for the reference condition, $Re = 3756$, in Secs. III B 1 and IIII B 2.

As discussed in Sec. III B 1, the occurrence of a radial velocity stagnation point at the endwell results in a local flow separation, and in the formation of a "von Kármán bubble," characterized by opposite direction of all the velocity components with respect to the bulk flow. This stagnation point and resulting boundary layer separation are from here onward referred to as "primary" because their occurrence and cascade of events thereafter were observed for all conditions studied. For some higher Re, the onset of following radial velocity stagnation points in the boundary layer, leading to further separation, is reported in this section, and they are referred to as "secondary."

Figures 10(a)–10(c) show the instantaneous profile of the radial velocity component within the endwall boundary layer (at $z/R = 0.04$) at the instant of primary boundary layer separation for
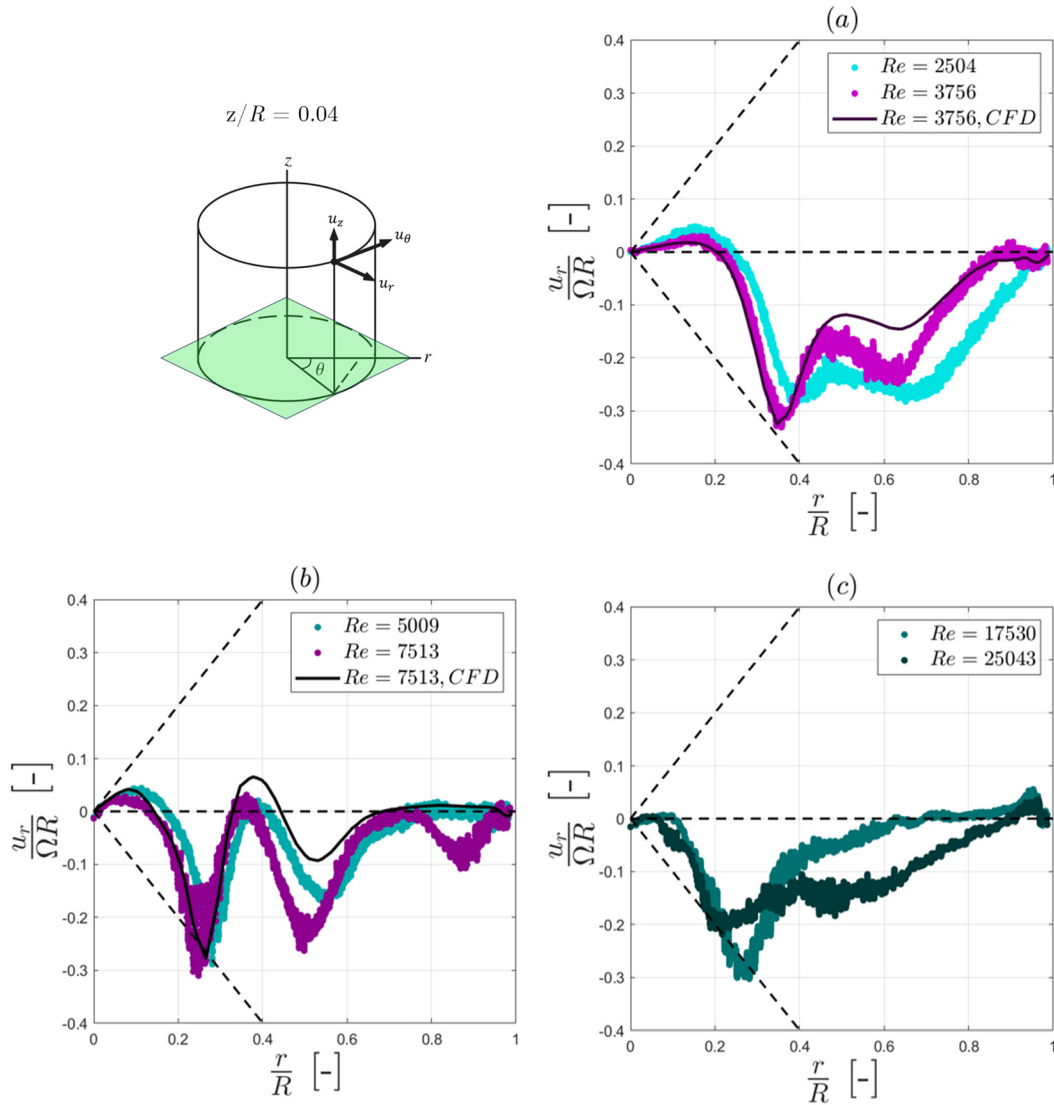
$Re = 2504$ and 3756 [Fig. 10(a)], $Re = 5009$ and 7513 [Fig. 10(b)], and $Re = 17\,530$ and $25\,043$ [Fig. 10(c)]. The moment of primary separation at different Re was identified by going through the data in increments of 0.1 s, and finding the profile of the radial velocity first exhibiting a positive value (i.e., outward flow region). This was found to occur at roughly the same instant across the range of Re investigated, $\Omega t \approx 2.9$. As already mentioned in Sec. III B 1 the separation at this height is delayed with respect to that occurring at the endwell ($\Omega t = 2.36$) where it first originates. The dimensional time difference between $\Omega t = 2.36$ and 2.9 at this Re is 0.3 s. Experimental conditions, for which computational results are available ($Re = 3756$ and 7513), are plotted with magenta markers and the corresponding CFD profile is illustrated with a solid black curve. The dashed solid lines indicate the tangential velocity profile at solid body rotation in each direction.

In Fig. 10, it is immediately noticeable that the first stagnation point (i.e., the innermost one), where the radial velocity changes sign and the endwall boundary layer locally transitions from Bödewadt to von Kármán type, occurs at smaller radii, R_{s1}, with increasing Re. This is also confirmed by the computational results, which are in very good agreement with the corresponding experimental profiles at $Re = 3756$ and $Re = 7513$.

In Figures 10(a)–10(c), it is seen that the shape of the radial velocity profiles is similar for conditions plotted in the same subfigure, however it changes between a), b) and c). For $Re = 5009$ and $Re = 7513$ [Fig. 10(b)], a secondary separation is also observed (simultaneously with the primary) at $R_{s2} = 0.38$ and 0.33, respectively. The secondary stagnation points occur ahead (radially inward) of the second radial wave, which is identified by the local minimum of the radial velocity at $r/R = 0.55$ at $Re = 5009$ and 0.5 at $Re = 7513$. On the other hand, for $Re = 2504$ and $Re = 3756$ [Fig. 10(a)], the second
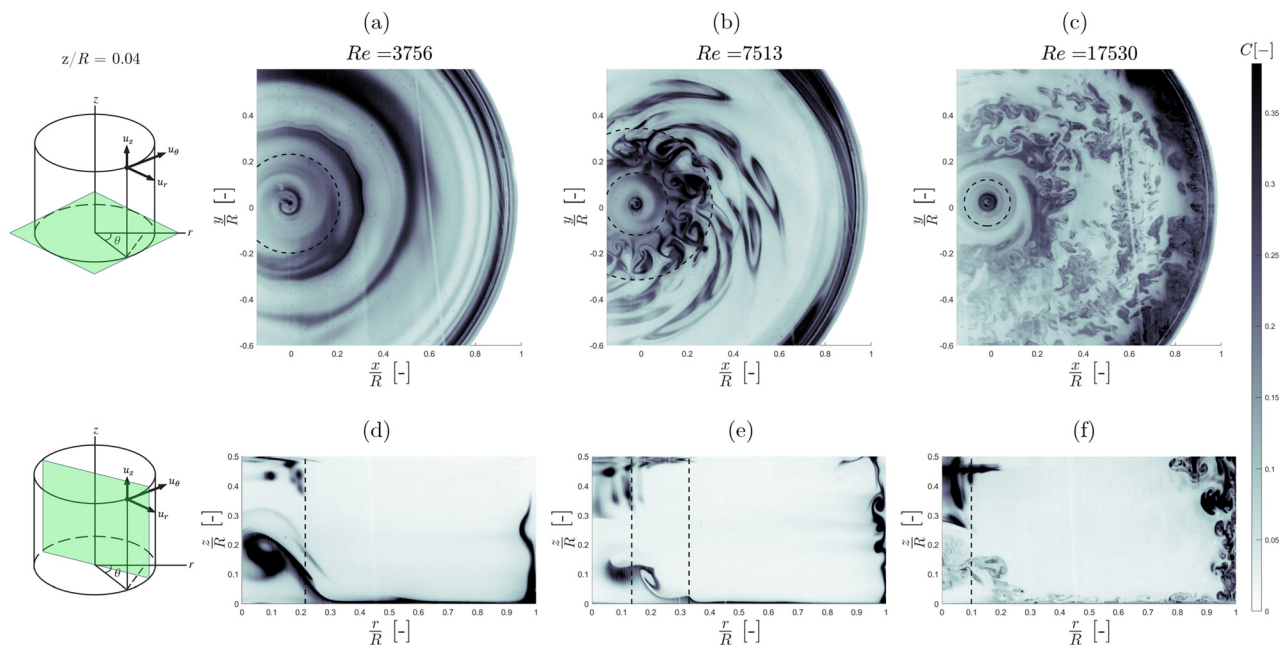
FIG. 9. PLIF images of the endwall boundary layer in the horizontal plane at $z/R = 0.04$ at the moment of primary boundary layer separation, $\Omega t \approx 2.9$: (a) $Re = 3756$; (b) $Re = 7513$; (c) $Re = 17\,530$; PLIF images of the vertical cross section at $\Omega t \approx 2.9$; (d) $Re = 3756$; (e) $Re = 7513$; and (f) $Re = 17\,530$. The dashed circles in (a)–(c) and vertical lines in (d)–(f) indicate the primary stagnation point radius, R_{s1} (and secondary stagnation point radius, R_{s2}, only for $Re = 7513$). Multimedia available online.

FIG. 10. Profiles of the radial velocity at $z/R = 0.04$ from PIV (markers) and CFD (solid curves) shortly after the moment of primary endwall boundary layer separation, $\Omega t = 2.9$: (a) $Re = 2504$ and 3756; (b) $Re = 5009$ and 7513; and (c) $Re = 17\,530$ and 25 043.

radial wave is further out in comparison, with the local minimum of radial velocity occurring at $r/R = 0.65$ and 0.62, respectively. The radial velocity ahead of the wave is increasing (becoming less negative), however fluid is still moving radially inward, and the secondary separation at R_{s2} is yet to occur. This indicates that while the primary separation arises at the same number of revolutions after the reversal of rotation for the range of Re considered, the secondary separation, resulting from the second radial wave, occurs later for lower Re as the propagation of the wave is delayed. For example, this is evident when directly comparing the contour plot and velocity profiles in Fig. 8 for $Re = 3756$ to the velocity profiles in Fig. 10(b) for $Re = 5009$ and 7513. In Fig. 8, the second wave has propagated inward beyond $r/R = 0.5$ at $\Omega t = 4.24$, while as previously mentioned for $Re = 5009$

and 7513 [Fig. 10(b)] the second wave has already formed within a circle of $r/R \leq 0.4$ at $\Omega t = 2.9$.

At the two highest Re (17 530 and 25 043) in Fig. 10(c), the formation of circular type II waves was not observed, and the radial velocity profiles do not show a pronounced second minimum, characteristic of the second radial wave. Due to the high rotation speeds, the boundary layer becomes turbulent and the structures produced are very fine, beyond the spatial resolution of the PIV system used. Therefore, PLIF was used to gain further insight into the early stages of spin-over at higher Re. The corresponding data are presented in Fig. 9.

Figures 9(a)–9(c) show PLIF images of the endwall boundary layer at $z/R = 0.04$ for $Re = 3756$ (multimedia available online), 7513 (multimedia available online), 17 530 (multimedia available online),

respectively, at the moment of primary boundary layer separation, $\Omega t \approx 2.9$. Figures 9(d)–9(f) display images of the vertical cross section at the same instant in time for $Re = 3756$ (multimedia available online), 7513 (multimedia available online), 17 530 (multimedia available online), respectively. The dashed circles in Figs. 9(a)–9(c) and lines in Figs. 9(d)–9(f) indicate the radial coordinate of the stagnation point, R_{s1}, for the corresponding Re, as measured in Fig. 10. For $Re = 7513$, the secondary stagnation radius, R_{s2}, is also indicated, as the secondary separation occurs simultaneously with the primary [see Figures 9(b) and 9(e)].

All images in Fig. 9 show the time of formation of the "von Kármán bubble" in the endwall boundary layer, which is identified by a stagnation point at R_{s1} and always occurs at $\Omega t \approx 2.9$ in the PIV plane considered ($z/R = 0.04$) for the range of Re. However, at $Re = 3756$, this is before the onset of spiral waves, as seen in Fig. 9(a) (and Fig. 8). For $Re = 7513$, it is around the onset of spiral waves, which are visualized in the horizontal cross section in Fig. 9(b). At this Re rolls of dye are seen to form at the high-shear interface between counter- and co-rotating fluid, resulting from the onset of the second radial wave and secondary separation (indicated by the outer dashed circle). At the highest, $Re = 17 530$, spiral waves were observed to occur immediately after the reversal of rotation, and by $\Omega t \approx 2.9$, the endwall boundary layer had transitioned to three-dimensional turbulence, as seen in Fig. 9(c). This transition to turbulence was only observed at the highest two Re (17 530 and 25 043) and can explain why the radial velocity profiles at the moment of primary separation in Fig. 10(c) generally have a different shape than the others, where radial waves were observed. They are also less smooth, as the onset of spiral waves and turbulence breaks the axisymmetry of the flow and generates variation in the radial component at a given radius, similarly to the discussion in Fig. 2. In the vertical cross section, Figures 9(d) and 9(e), the transition to turbulence at $Re = 17 530$ is evident both in the endwall boundary layer, where multiple turbulent rolls of dye are visible, and in the sidewall boundary layer, where the T–G vortices, which are in their early formation stage at $Re = 7513$, have also transitioned to turbulence at $Re = 17 530$. These transitions are well captured by the corresponding multimedia available online.

Figures 11(a) and 11(b) provide a clear view of how the onset time and first radial location, R_{s1}, of the primary stagnation point vary with Reynolds number, respectively. Data-points were obtained from CFD as well PIV datasets. For reference, the dashed line in Fig. 11(a) visualizes the onset time of singularity in the boundary layer, according to the analytical model of Stewartson et al.[43] It corresponds to a constant number of revolutions (in radians), equal to 2.36 (i.e., $\Omega t = 2.36$).

When the onset time of primary separation is considered [see Fig. 11(a)], it is evident that the experimental PIV data (cyan squares) are notably parallel to the analytical model[43] (dashed cyan line), albeit a little higher. This confirms the earlier observation that the onset of primary separation, found from the PIV radial velocity profiles at an elevation of $z/R = 0.04$, is slightly delayed with respect to the endwall and occurs at a constant number of revolutions after the reversal of rotation ($\Omega t = 2.9$) for the range of Re investigated (see Fig. 10). This is further substantiated by the remarkable agreement between Stewartson's analytical model and the CFD data points (blue squares), which were obtained from radial velocity profiles closer to the endwell ($z/R = 0.01$).

Similarly to the onset time, the normalized radial coordinate of the first stagnation point, plotted in Fig. 11(b), also decreases with increasing Re, indicating that the diameter of the "von Kármán bubble," which appears at the axis of rotation is smaller at higher Re.

C. Sidewall boundary layer

This section focuses on the onset of centrifugal instabilities in the sidewall boundary, namely the Taylor–Görtler vortices, which represent a significant part of the flow during spin-over. PIV results for the vorticity of the Taylor–Görtler vortices from the vertical midplane are presented alongside CFD data, and spin-over is compared to spin-down.

Figure 12 illustrates a contour plot of the instantaneous tangential vorticity ω_θ/Ω, at $\Omega t = 4.4$, in the vertical midplane for spin-over at $Re = 7513$, $Fr = 0.1$. Figure 12(a) shows computational data and Fig. 12(b) illustrates PIV data. The corresponding axial profiles of the tangential vorticity are provided in Fig. 12(c), comparing data from
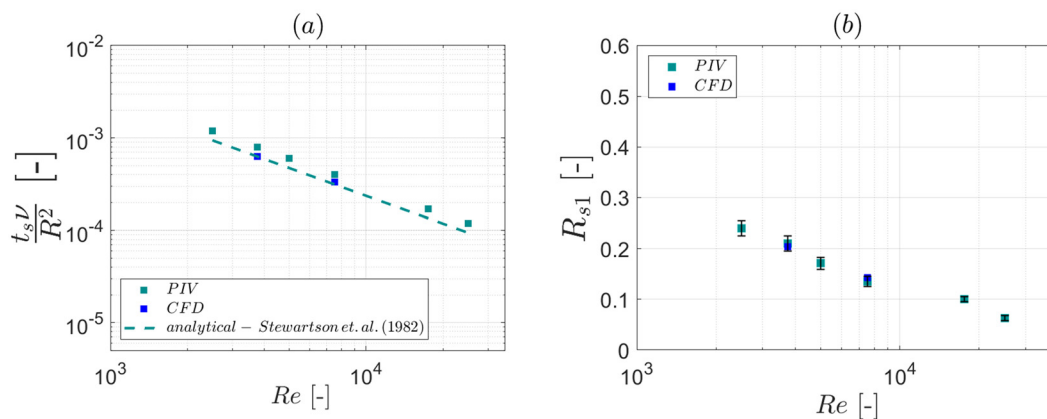
FIG. 11. (a) Onset time of the primary stagnation point in the endwall boundary layer during spin-over, $t(R_{s1})$, obtained with PIV (cyan squares) and CFD (blue squares) for different Re. The dashed cyan line shows the onset of a singularity in the boundary layer over a rotating disk in a counter-rotating fluid, according to the analytical model of Stewartson et al.[43] (b) First radial location of the primary stagnation point in the endwall boundary layer, R_{s1}, obtained from PIV (cyan) and from CFD (blue).
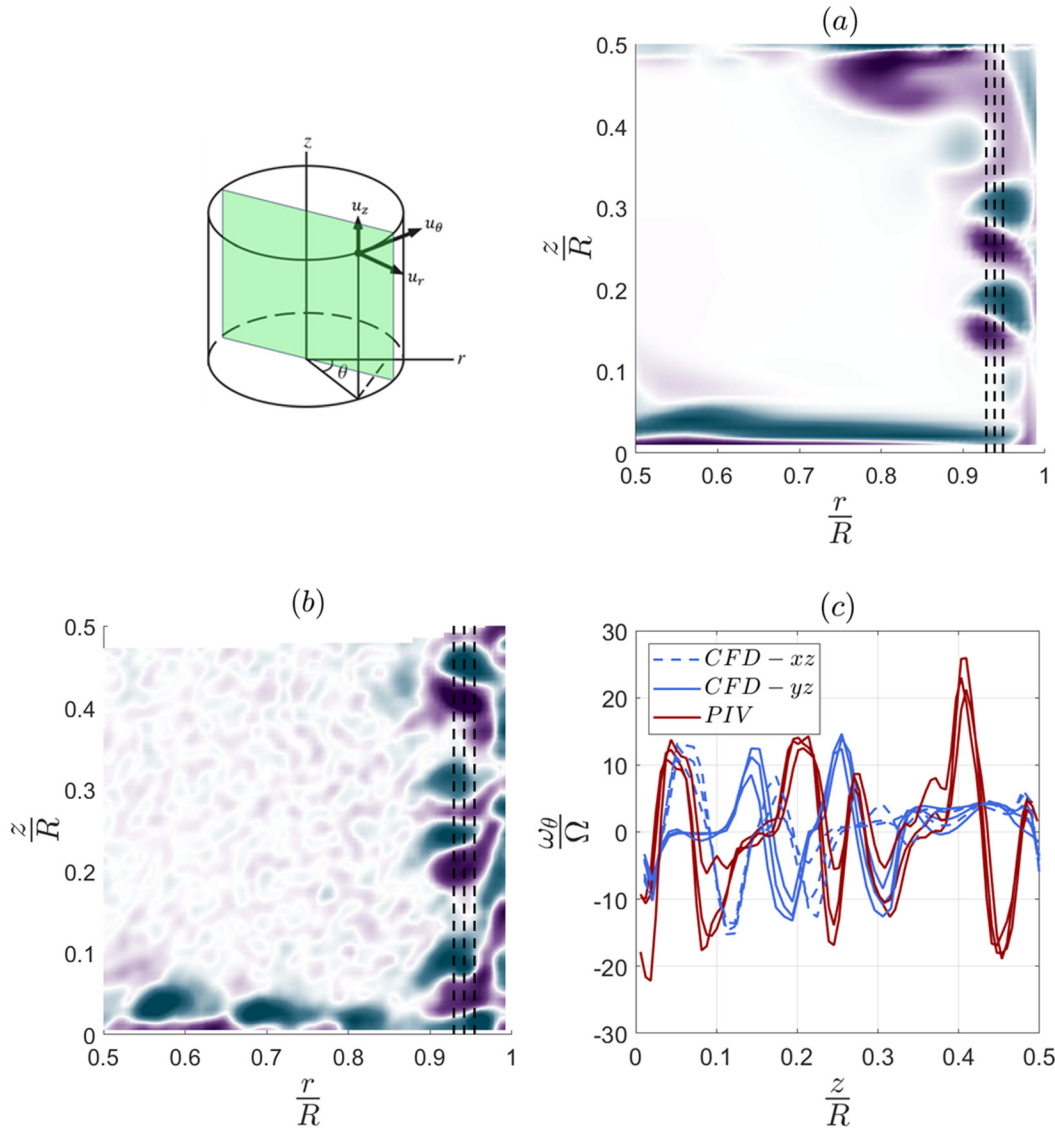
FIG. 12. Contour plots of the instantaneous tangential vorticity, ω_θ/Ω, in the vertical cross section at $\Omega t = 4.4$ for $Re = 7513$: (a) CFD and (b) PIV; (c) axial profiles of the instantaneous tangential vorticity from PIV (magenta) and CFD (cyan) at three radial locations, as indicated by the vertical dashed lines in (a) and (b). The solid cyan curves show data from the CFD cross section shown in (a), yz, while the dashed cyan curves show CFD data from a second vertical cross section, xz, at 90° to yz.

PIV (magenta) and CFD (cyan) at three radial positions, $r/R \approx 0.93$, 0.94, and 0.95 [see vertical dashed lines in Figures 12(a) and 12(b)]. To account for the variability in the formation and axial location of the T–G vortices in the azimuthal direction, θ, two sets of computational profiles were extracted from two different vertical half cross sections, denoted as xz and yz, orthogonal to each other. Data in the yz plane (Cartesian coordinate system) are visualized in the contour plot [Fig. 12(a)] and presented as solid (cyan) lines in Fig. 12(c), whereas profiles from the xz plane (contour plot not shown) are represented by dashed (cyan) lines.

The presence of Taylor–Görtler instabilities, manifesting as pairs of counter-rotating vortices, is evident near the sidewall at $\Omega t = 4.4$,

from both CFD [Fig. 12(a)] and PIV [Fig. 12(b)] data. While some variation in the shape and structure is inevitable due to the transient and unstable nature of the flow, there is very good agreement between the simulation and the experiments, with both displaying a similar number of T–G vortex pairs of comparable size and vorticity magnitude at the same instant in time. In Fig. 12(c), a second computational plane was examined, xz, orthogonal to the one shown in Fig. 12(a), to examine the variation of the vortices along the circumference of the cylinder at a given instant. It is seen that their structure exhibits some variability with the azimuthal coordinate, θ, with a vortex pair being present near the bottom at $0.05 \leq z/R \leq 0.1$ in the xz plane (dashed cyan line), seen also in the experimental plane (magenta), whereas no such pair is

12 December 2024 08:31:25

present in the yz computational plane (solid cyan line). Despite the chaotic nature of the flow, the agreement of the CFD and experimental data is particularly highlighted by the common onset time and range of vorticity magnitude at the same instant.

To visualize the development of the T–G vortices in time, Fig. 13 illustrates an example of the instantaneous normalized vorticity, $\frac{\omega_\theta}{\Omega}$, in the vertical cross section at different instants in Ekman time, T, and for different Re (PIV data).

In Fig. 13, it is seen that during spin-over the onset of T–G vortices occurs earlier, and the pairs appear smaller with increasing Re, similarly to spin-down (cf. Fig. 6 in Ref. 22). The different-sized primary pairs of counter-rotating T–G vortices can be seen in Fig. 13 at $T = 0.059$ and 0.066 for $Re = 5009$, at $T = 0.031$ for $Re = 10\,017$, and at $T = 0.018$ for $Re = 15\,026$. The instabilities first appear small in the vertical cross section, and the diameter of a vortex pair is seen to increase in size, before the vortices lose their structured shape and the local flow transitions to turbulence (e.g., $T = 0.083$, 0.059, and 0.031 from low to high Re). In comparison to analogous data for spin-down to rest,[22] it is seen that the endwall boundary layer during spin-over experiences separation, unlike spin-down, and the magnitude of vorticity is higher (by a factor of 1.3–1.4). High vorticity is also observed in the interior during spin-over, which is absent during spin-down,

where the interior fluid above the endwall boundary layer can be approximated as inviscid.

Noticeably, the onset time and transition to turbulence occur at a slightly lower but very similar time during spin-over, as they do during spin-down at the same Re. The size and number of vortex pairs formed is also similar between the two processes at a given Re.

To better illustrate the difference in vorticity magnitude between spin-over and spin-down, the vorticity of the T–G vortices was isolated using the λ_2 technique. A negative threshold was used for λ_2 (as opposed to 0) in order to separate the vorticity of the T–G instabilities from random velocity gradients due to experimental noise.

$$
\hat{\omega}_\theta =
\begin{cases}
\dfrac{\omega_\theta}{\Omega} & \text{when } \lambda_2 < -6.5\left(\dfrac{2\Omega}{\pi}\right)^2, \\[3ex]
0 & \text{when } \lambda_2 \geq -6.5\left(\dfrac{2\Omega}{\pi}\right)^2.
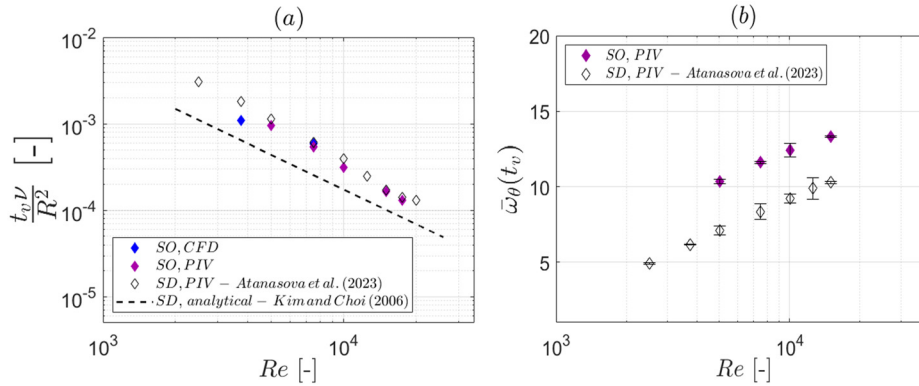\end{cases}
\tag{15}
$$

The area-weighted instantaneous tangential vorticity is then defined as

$$
\overline{\omega}_\theta(t) = \frac{1}{\mathscr{S}} \int \hat{\omega}_\theta(t)\, dA,
\tag{16}
$$

where $\mathscr{S}$ is the cross-sectional area in the rz-plane.
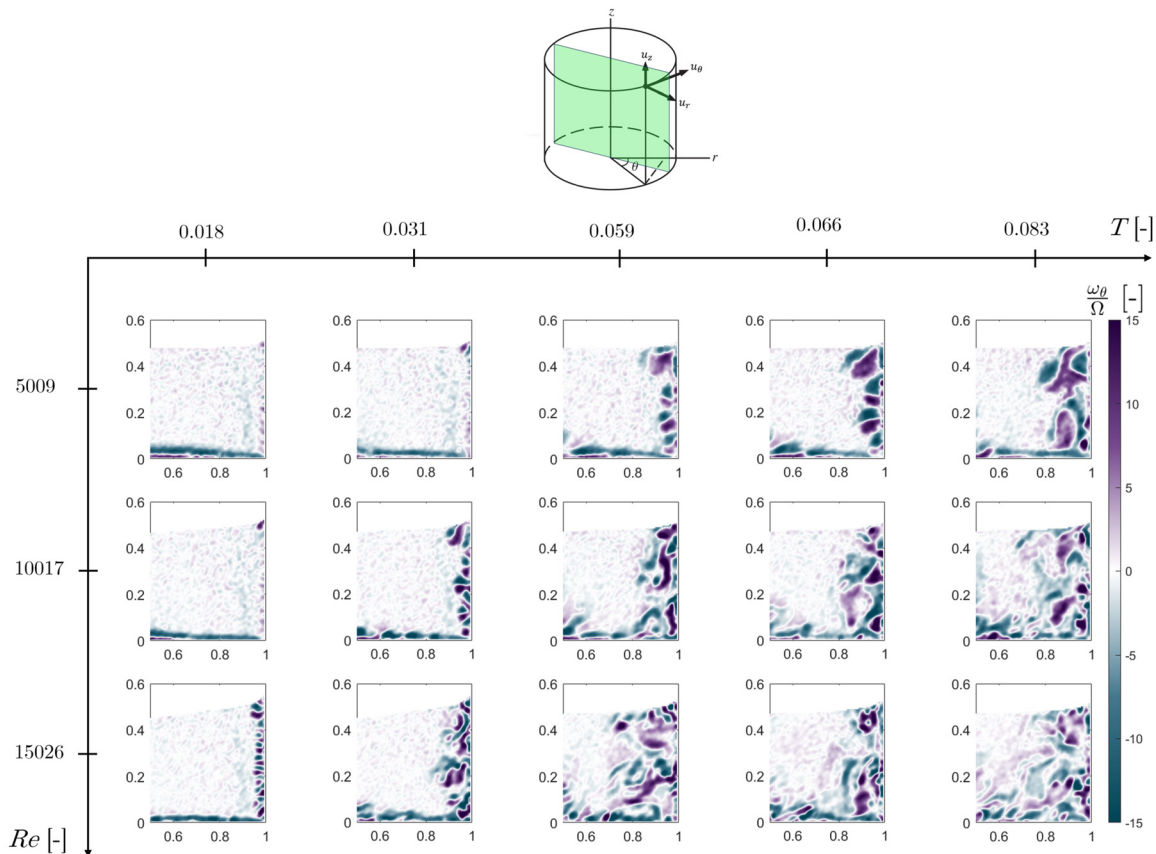
FIG. 13. Contour plot of the instantaneous tangential vorticity, ω_θ/Ω, in the vertical midplane, obtained with PIV, illustrating the onset and transition to turbulence of the Taylor–Görtler vortices; The x-axis shows the trend with increasing Ekman time, T, and the y-axis shows the trend with increasing Reynolds number, Re. The field of view is $r/R = 0.5$–1, $z/R = 0$–0.5.

FIG. 14. (a) Onset time of the Taylor–Görtler vortices during spin-down (SD, empty diamonds) and spin-over (SO, filled diamonds), obtained with PIV (magenta) and CFD (blue). (b) Peak magnitude of the area-weighted vorticity, $\overline{\omega}_\theta(t_v)$, of the T–G vortices during spin-over (magenta) and spin-down (empty diamonds from Ref. 22).

The area-weighted instantaneous tangential vorticity is zero at the beginning of spin-over, then rapidly increases with the first appearance of the T–G vortices at the sidewall and reaches a maximum when they have grown radially inward to form the large structured pairs visible at $T = 0.059$ and 0.066 for $Re = 5009$, at $T = 0.031$ for $Re = 10\,017$, and at $T = 0.018$ for $Re = 15\,026$ in Fig. 13. The time at which the area-weighted vorticity peaks, t_v, is used to characterize the onset time of the vortices at different Re and is plotted in Fig. 14(a). After this time, the T–G instabilities transition to turbulence, the structured pairs are no longer visible, and the area-weighted vorticity begins decaying steadily in time.

Figures 14(a) and 14(b) provide a direct comparison between the Taylor–Görtler instabilities observed during spin-over and those present during spin-down (extracted from Ref. 22) in terms of instability onset time, t_v, and maximum magnitude of the area-weighted vorticity, $\overline{\omega}_\theta(t_v)$, for different Reynolds numbers. For reference, the dashed line in Fig. 14(a) represents the analytical model derived by Kim and Choi[31] for the onset time of the vortices on the sidewall during spin-down. The slight time delay in onset time between the model and the data presented here is due to the definition of onset time, which in this work was identified as the instant when the area-weighted vorticity reaches its maximum value. This delay accounts for the growth of the vortices, which expand from the sidewall to the interior of the reactor. To put this in context, reflective flakes measurements reported by Atanasova et al.[22] fully capture the first formation of the T–G vortices on the cylinder sidewall and match closely the analytical model of Kim and Choi[31]. When comparing spin-over to spin-down for same onset time definition, it is clear that spin-over (magenta diamonds) shows a slightly earlier onset time compared to spin-down (empty diamonds), more prominent at $Re < 10\,000$. However the trend with Re, illustrated by the slope of the points, is very similar between spin-down and spin-over. Experimental and computational data for spin-over (magenta and blue diamonds, respectively) are in close agreement.

A major difference between the two process arises from the maximum area-weighted vorticity in Fig. 14(b), which indicates more intense T–G instabilities during spin-over by a factor of ≈ 1.3–1.4 across the range of Reynolds investigated. This aspect is particularly important for the promotion of enhanced mixing on the finer scales of the bioreactor.

IV. CONCLUSIONS

While prior investigations have explored spin-over phenomena across different geometries, a gap in the literature persists regarding the spin-over of a fluid confined to a cylinder with an intermediate aspect ratio and a free surface. The present study stands as an effort to bridge this gap, presenting a comprehensive analysis of the intricate transient flow dynamics within a partially filled cylinder with liquid height to radius ratio, $L/R = 0.5$, rotating at solid body rotation (SBR), which impulsively reverses its direction of rotation. This work offers a combination of novel experimental results from particle image velocimetry (PIV) and planar laser-induced fluorescence (PLIF), alongside transient three-dimensional computational fluid dynamics (CFD) data, which provide insight into the interior flow, the behavior of the endwall and sidewall boundary layers and how they evolve in time.

The study revealed a significant distinction between the early stages of spin-over and the traditional spin-down to rest. Unlike the latter, the interior fluid no longer maintains solid body rotation during spin-over and experiences a notably faster loss of angular momentum. The combined instantaneous tangential flux, accounting for both rotation in the positive (original) and the negative (new) direction, decreases to approximately 15%–36% of its solid body rotation value within an Ekman time interval of $T = 0.26$–0.6, while analogous losses would occur over an Ekman time period of about 2.5 in spin-down. This aspect was valid across the entire range of Reynolds numbers investigated, $2504 < Re < 25\,043$, with a lower decline observed at higher Reynolds numbers. Following this stage, the fluid begins to regain angular momentum in the new direction. Around that point, a flow which resembles the geostrophic flow during spin-up is established, and the fluid attains angular momentum until it reaches solid body rotation in the new direction.

Subsequent analysis of the endwall boundary layer revealed a complex sequence of fluid dynamics events, which begins with the formation of a radial velocity stagnation point (i.e., only $u_r = 0$) in the endwall boundary layer at $r_{s1}/R = R_{s1}$, and results in the disruption of the rigidly rotating core of fluid above the endwall boundary layer. Computational and experimental results were in excellent agreement. The stagnation point was robustly detected at the same number of revolutions after the change of rotation for the range of Re considered (2504–25 043), at $\Omega t = 2.36$ from CFD data at $z/R = 0.01$) and at $\Omega t \approx 2.9$ from PIV at $z/R = 0.04$. This resulted in the transition of the inner endwall boundary layer from Bödewadt to von Kármán type, and the formation of a "von Kármán bubble," a distinct bubble-shaped region around the axis of rotation, close to the bottom, with opposite circulation to the main flow [see Fig. 7(a)]. This confined von

Kármán-type region was seen to expand axially upward and then to detach from the endwall [see Fig. 7(b)]. It briefly remained in the interior as a free shear layer, traveling upward and eventually dissipated around the axis of rotation, reaching all the way to the free surface. This resulted in substantial modifications to the core flow and the generation of multiple secondary circulation flow cells and very efficient transport of the fluorescent dye across the entire interior, rather than it being confined to the boundary layers as in the case of spin-down.

In the later stages of spin-over, circular radial waves and stationary spiral waves were observed, resembling the type II and type I instabilities, respectively, characteristic of Bödewadt boundary layers; however, they had inverse radial and tangential velocity components, aligned with the rotation of the wall in the new direction. The wave instabilities resulted in the onset of more stagnation radial points in the endwall boundary layer, occurring further radially out. At $Re > 17\,530$, the circular waves were no longer seen, but instead spiral waves appeared almost instantaneously after the change of rotation, leading the boundary layer to transition to turbulence [i.e., Fig. 9(a)]. With increasing Re, the primary stagnation radius, R_{s1}, was found to decrease. The onset and behavior of the Taylor–Görtler vortices, generated in the sidewall boundary layer, were also examined and compared to spin-down to rest. Experimental and computational results were again in very good agreement. It was found that their onset occurs slightly earlier during spin-over, and their maximum vorticity is significantly higher (by a factor of 1.3–1.4), which could also contribute to the faster loss of angular momentum during the early stages of spin-over.

In the context of mixing in an intermittently rotating cylindrical bioreactor, implementing spin-over steps into the rotation pattern is likely to offer greater benefits compared to spin-down, due to the efficient recirculation of the interior fluid, as a result of the endwall boundary layer separation and formation of the "von Kármán bubble," as well as the higher vorticity in the sidewall boundary layer. In addition, it appears spin-over would be particularly advantageous for suspending cells within the liquid, owing to the strong axial upward flow along the rotation axis during the formation of the first stagnation point and endwall boundary layer separation. These features of the flow are crucial for mixing, oxygen mass transfer, and solids resuspension, making spin-over a better alternative than both spin-up and spin-down for cell growth, although at the cost of increased power consumption and shear stress, which may be detrimental to more sensitive cells.

In summary, this study offers a detailed account of the flow during spin-over in a partially filled cylinder with an intermediate aspect ratio ($L/R = 0.5$) and provides insight into previously unexplored features of transient confined rotating flows with a free surface. The presented findings have a broad range of applications, from mixing in rotating bioreactors for advanced therapies manufacturing, to geophysical systems and turbo-machinery.

ACKNOWLEDGMENTS

AUTHOR DECLARATIONS
Conflict of Interest

The authors have no conflicts to disclose.

Author Contributions

Gergana G. Atanasova: Conceptualization (equal); Data curation (lead); Formal analysis (equal); Investigation (lead); Methodology (lead); Validation (lead); Visualization (lead); Writing – original draft (lead); Writing – review & editing (lead). **Christian A. Klettner:** Formal analysis (equal); Investigation (equal); Software (equal); Supervision (equal); Writing – review & editing (equal). **Martina Micheletti:** Funding acquisition (lead); Resources (equal); Supervision (equal); Writing – review & editing (supporting). **Andrea Ducci:** Conceptualization (equal); Data curation (equal); Investigation (equal); Project administration (equal); Supervision (equal); Writing – original draft (equal); Writing – review & editing (supporting).

DATA AVAILABILITY

The data that support the findings of this study are available from the corresponding author upon reasonable request.

REFERENCES

[1]H. Goller and T. Ranov, "Unsteady rotating flow in a cylinder with a free surface," J. Basic Eng. **90**, 445–454 (1968).

[2]J. M. Floryan, "On the Görtler instability of boundary layers," Prog. Aerosp. Sci. **28**, 235–271 (1991).

[3]W. Munk, "Spirals on the sea," Sci. Mar. **65**, 193–198 (2001).

[4]J. Lopez, F. Marques, A. M. Rubio, and M. Avila, "Crossflow instability of finite Bödewadt flows: Transients and spiral waves," Phys. Fluids **21**, 1–9 (2009).

[5]K. M. Cappell and J. N. Kochenderfer, "Long-term outcomes following CAR-T cell therapy: What we know so far," Nat. Rev. Clin. Oncol. **20**, 359–371 (2023).

[6]M. P. Gustafson, J. A. Ligon, A. Bersenev, C. D. McCann, N. N. Shah, and P. J. Hanley, "Emerging frontiers in immuno- and gene therapy for cancer," Cytotherapy **25**, 20–32 (2023).

[7]N. El-Khazragy, S. Ghozy, P. Emad, M. Mourad, D. Razza, Y. K. Farouk, N. A. Mohamed, M. K. Ahmed, T. Youssef, Y. M. Bahnasawy, and S. Elmasery, "Chimeric antigen receptor t cells immunotherapy: Challenges and opportunities in hematological malignancies," Immunotherapy **12**, 1341–1357 (2020).

[8]U. Mock, L. Nickolay, B. Philip, G. W. K. Cheung, H. Zhan, I. C. D. Johnston, A. D. Kaiser, K. Peggs, M. Pule, A. J. Thrasher, and W. Qasim, "Automated manufacturing of chimeric antigen receptor T cells for adoptive immunotherapy using clinimacs prodigy," Cytotherapy **18**, 1002–1011 (2016), the Golden 1.

[9]A. Charalambidou, T. A. Wyrobnik, M. Micheletti, and A. Ducci, "Investigation of the impact of probes and internals on power and flow in stirred tank reactors," Chem. Eng. Sci. **286**, 119683 (2024).

[10]H. P. Greenspan, *The Theory of Rotating Fluids* (Cambridge University Press, 1968).

[11]H. Schlichting and K. Gersten, *Boundary-Layer Theory*, 9th ed. (Springer, 2017), pp. 355–358.

[12]E. H. Wedemeyer, "The unsteady flow within a spinning cylinder," J. Fluid Mech. **20**, 383–399 (1964).

[13]H. P. Greenspan and L. N. Howard, "On a time-dependent motion of a rotating fluid," J. Fluid Mech. **17**, 385–404 (1963).

[14] S. Choi, J. W. Kim, and J. M. Hyun, "Experimental investigation of the flow with a free surface in an impulsively rotating cylinder," J. Fluids Eng. **113**, 245–249 (1991).

[15] P. D. Weidman, "On the spin-up and spin-down of a rotating fluid. Part 2. Measurements and stability," J. Fluid Mech. **77**, 709–735 (1976).

[16] O. Savaş, "On flow visualization using reflective flakes," J. Fluid Mech. **152**, 235–248 (1985).

[17] W. B. Watkins and R. G. Hussey, "Spin-up from rest in a cylinder," Phys. Fluids **20**, 1596–1604 (1977).

[18] C. W. Kitchens, "Navier-Stokes solutions for spin-up in a filled cylinder," AIAA J. **18**, 929–934 (1980).

[19] G. Homicz and N. Gerber, "Numerical model for fluid spin-up from rest in a partially filled cylinder," J. Fluids Eng. **109**, 194–197 (1987).

[20] R. C. Kloosterziel and G. J. F. van Heijst, "The evolution of stable barotropic vortices in a rotating free-surface fluid," J. Fluid Mech. **239**, 607–629 (1992).

[21] J. O'Donnell and P. F. Linden, "Free-surface effects on the spin-up of fluid in a rotating cylinder," J. Fluid Mech. **232**, 439–453 (1991).

[22] G. G. Atanasova, M. Micheletti, and A. Ducci, "Fluid flow and mixing in a novel intermittently rotating bioreactor for CAR-T cell therapy manufacturing," Chem. Eng. Sci. **281**, 119175–119116 (2023).

[23] M. Dauth and N. Aksel, "Breaking of waves on thin films over topographies," Phys. Fluids **30**, 082113 (2018).

[24] M. Dauth and N. Aksel, "Transition of regular wave fronts to irregular wave fronts in gravity-driven thin films over topography," Acta Mech. **230**, 2475–2490 (2019).

[25] G. P. Neitzel and S. H. Davis, "Centrifugal instabilities during spin-down to rest in finite cylinders. Numerical experiments," J. Fluid Mech. **102**, 329–352 (1981).

[26] G. P. Neitzel and S. H. Davis, "Energy stability theory of decelerating swirl flows," Phys. Fluids **23**, 432–437 (1980).

[27] F. Kaiser, B. Frohnapfel, R. Ostilla-Mónico, J. Kriegseis, D. E. Rival, and D. Gatti, "On the stages of vortex decay in an impulsively stopped, rotating cylinder," J. Fluid Mech. **885**, A6 (2020).

[28] A. I. van de Vooren, "The connection between Ekman and Stewartson layers for a rotating disk," J. Eng. Math. **27**, 189–207 (1993).

[29] D. M. Mathis and G. P. Neitzel, "Experiments on impulsive spin-down to rest," Phys. Fluids **28**, 449–454 (1985).

[30] X. Cui, "Numerical simulations of the generation of Taylor-Görtler vortices during spin-down to rest infinite-length cylinders," Comput. Fluids **33**, 603–621 (2004).

[31] M. C. Kim and C. K. Choi, "The onset of Taylor-Görtler vortices during impulsive spin-down to rest," Chem. Eng. Sci. **61**, 6478–6485 (2006).

[32] G. Euteneuer, "Störwellenlängen-Messung bei Längswirbeln in laminaren Grenzschichten an konkav gekrümmten Wänden," Acta Mech. **7**, 161–168 (1968).

[33] G. Euteneuer, "Die Entwieklung von Längswirbeln in zeitlich anwachsenden Grenzschichten an konkaven Wänden," Acta Mech. **13**, 215–223 (1972).

[34] T. Maxworthy, "The structure and stability of vortex rings," J. Fluid Mech. **51**, 15–32 (1972).

[35] G. G. Atanasova, A. Ducci, and M. Micheletti, "Fluid dynamics and mixing in a novel intermittently rotating bioreactor for CAR-T cell therapy: Spin-down from incomplete spin-up," Chem. Eng. Res. Des. **205**, 486–497 (2024).

[36] A. J. Faller, "An experimental study of the instability of the laminar Ekman boundary layer," J. Fluid Mech. **15**, 560–576 (1963).

[37] A. J. Faller, "Instability and transition of disturbed flow over a rotating disk," J. Fluid Mech. **230**, 245–269 (1991).

[38] O. Savaş, "Stability of Bödewadt flow," J. Fluid Mech. **183**, 77–94 (1987).

[39] O. Savaş, "Spin-down to rest in a cylindrical cavity," J. Fluid Mech. **234**, 529–552 (1992).

[40] J. M. Lopez and P. D. Weidman, "Stability of stationary endwall boundary layers during spin-down," J. Fluid Mech. **326**, 373–398 (1996).

[41] R. J. Bodonyi and K. Stewartson, "The unsteady laminar boundary layer on a rotating disk in a counter-rotating fluid," J. Fluid Mech. **79**, 669–688 (1977).

[42] R. J. Bodonyi, "On the unsteady similarity equations for the flow above a rotating disc in a rotating fluid," Q J. Mech. Appl. Math. **31**, 461–472 (1978).

[43] K. Stewartson, C. J. Simpson, and R. J. Bodonyi, "The unsteady boundary layer on a rotating disk in a counter-rotating fluid. Part 2," J. Fluid Mech. **121**, 507–515 (1982).

[44] W. H. H. Banks and M. B. Zaturska, "The unsteady boundary-layer development on a rotating disc in counter-rotating flow," Acta Mech. **38**, 143–155 (1981).

[45] C. E. Pearson, "Numerical solutions for the time-dependent viscous flow between two rotating coaxial disks," J. Fluid Mech. **21**, 623–633 (1965).

[46] D. Dijkstra and G. J. V. Heijst, "The flow between two finite rotating disks enclosed by a cylinder," J. Fluid Mech. **128**, 123–154 (1983).

[47] G. Gauthier, P. Gondret, F. Moisy, and M. Rabaud, "Instabilities in the flow between co- and counter-rotating disks," J. Fluid Mech. **473**, 1–21 (2002).

[48] J. M. Lopez, "Characteristics of endwall and sidewall boundary layers in a rotating cylinder with a differentially rotating endwall," J. Fluid Mech. **359**, 49–79 (1998).

[49] J. M. Lopez, J. E. Hart, F. Marques, S. Kittelman, and J. Shen, "Instability and mode interactions in a differentially driven rotating cylinder," J. Fluid Mech. **462**, 383–409 (2002).

[50] L. Gamet, M. Scala, J. Roenby, H. Scheufler, and J.-L. Pierson, "Validation of volume-of-fluid OpenFOAM® isoAdvector solvers using single bubble benchmarks," Comput. Fluids **213**, 104722 (2020).

[51] H. G. Weller, G. Tabor, H. Jasak, and C. Fureby, "A tensorial approach to computational continuum mechanics using object-oriented techniques," Comput. Phys. **12**, 620–631 (1998).

[52] C. Hirt and B. Nichols, "Volume of fluid (vof) method for the dynamics of free boundaries," J. Comput. Phys. **39**, 201–225 (1981).

[53] J. Roenby, H. Bredmose, and H. Jasak, "A computational method for sharp interface advection," R. Soc. Open Sci. **3**, 160405 (2016).